

# **MIM based plasmonic Refractive Index (RI) sensor, Demultiplexer and Filter with Resonant Cavities.**

by

Tahmid Mahbub (170021040)

Qazi Mahabub-A-Rabbani (170021122)

Sakib Mahmud (170021139)

**BACHELOR OF SCIENCE  
IN  
ELECTRICAL AND ELECTRONIC ENGINEERING**



Department of Electrical and Electronic Engineering  
Islamic University of Technology (IUT)  
Board Bazar, Gazipur-1704, Bangladesh.  
May, 2022.

## Declaration of Authorship

We, Tahmid Mahbub (170021040), Qazi Mahabub-A-Rabbani (170021122) and Sakib Mahmud (170021139), state that this thesis titled, 'MIM based Plasmonic Refractive Index (RI) Sensor, Demultiplexer and Filter with Resonant Cavities' and the works that have been proposed completely belong to us. The works have mainly been done for the fulfillment of the Bachelor of Science at this university. No part of this work has been submitted elsewhere.

Tahmid Mahbub 31.05.22

Tahmid Mahbub (170021040)

Q Mahabub 31-05-22

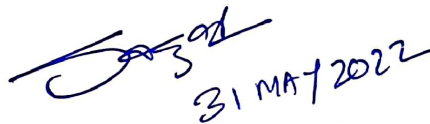
Qazi Mahabub-A-Rabbani (170021122)

Sakib Mahmud 31.5.22

Sakib Mahmud (170021139)

# **MIM based plasmonic Refractive Index (RI) sensor, Demultiplexer and Filter with Resonant Cavities.**

Approved by:



31 MAY 2022

---

Dr. Rakibul Hasan Sagor

Professor

Department of Electrical and Electronic Engineering

Islamic University of Technology (IUT)

Dhaka, Bangladesh

# Table of Contents

<b>Declaration of Authorship</b>	<b>i</b>
<b>List of Figures</b>	<b>vi</b>
<b>List of Tables</b>	<b>ix</b>
<b>List of Abbreviations</b>	<b>x</b>
<b>Acknowledgement</b>	<b>xi</b>
<b>Abstract</b>	<b>xii</b>
<b>1 Introduction and Background</b>	<b>1</b>
1.1 Surface Plasmon Polariton . . . . .	1
1.2 Plasmonic Devices . . . . .	2
1.2.1 Plasmonic Filter . . . . .	2
1.2.2 Plasmonic Demultiplexers . . . . .	3
1.2.3 Plasmonic Sensor . . . . .	4
1.3 Waveguide topology . . . . .	4
1.3.1 MIM waveguide . . . . .	4
1.3.2 IMI waveguide . . . . .	5
1.3.3 Hybrid waveguide . . . . .	6
1.4 Literature Review . . . . .	8
1.5 Thesis Objective . . . . .	16
1.6 Thesis Layout . . . . .	16
<b>2 Electromagnetic Wave Theory</b>	<b>18</b>
2.1 Maxwell's and Wave equations . . . . .	18
2.1.1 Maxwell's equations . . . . .	18
2.1.2 Constitutive equation . . . . .	19
2.1.3 Generalized Constitutive Equations (Non-Linear Materials) . . . . .	20
2.1.4 Wave Equation . . . . .	21
2.2 Simulation Modeling . . . . .	21

2.2.1	Finite Element Method . . . . .	21
<b>3</b>	<b>Plasmonic Materials</b>	<b>23</b>
3.1	Refractive Index and Complex Permittivity . . . . .	23
3.2	Material Modeling . . . . .	24
3.2.1	Drude Model . . . . .	24
3.2.2	Lorentz Model . . . . .	24
3.2.3	Lorentz-Drude Model . . . . .	24
3.3	Ag Modeling . . . . .	24
3.4	Au Modeling . . . . .	26
<b>4</b>	<b>Resimulation and Performance Metrics</b>	<b>27</b>
4.1	Resimulation for Quality validation . . . . .	27
4.1.1	Resimulation of Sensor . . . . .	27
4.1.2	Resimulation of Demultiplexer . . . . .	31
4.2	Performance Metrics . . . . .	33
4.2.1	Sensitivity (S) . . . . .	34
4.2.2	Figure of merit (FOM) . . . . .	35
4.2.3	Quality Factor (Q-factor) . . . . .	35
4.3	Ring and Cavity Resonator . . . . .	36
<b>5</b>	<b>Design, Optimization and Performance Analysis of the Proposed Devices</b>	<b>39</b>
5.1	Sensor Design with U shaped cavity coupled with a subannular circle . . . . .	39
5.1.1	Structure Layout . . . . .	39
5.1.2	Initial Transmission spectrum and results . . . . .	40
5.1.3	Optimization for gaining Maximum sensitivity . . . . .	43
5.1.4	Temperature sensor . . . . .	47
5.2	Filter design with triple ring resonators, each having triple stubs . . . . .	48
5.2.1	Structure layout . . . . .	48
5.2.2	Result analysis of double ring resonators . . . . .	50
5.2.3	Result analysis of double ring resonators with stubs . . . . .	52
5.2.4	Result analysis of triple ring resonator filter . . . . .	54
5.2.5	Result analysis of triple ring resonator filter with stubs . . . . .	56
5.3	Concentric ring and nanodisk resonator for wavelength multiplexing . . . . .	59
5.3.1	Structure Layout . . . . .	59
5.3.2	Initial Transmission spectrum and results . . . . .	60
5.3.3	Improving the channeling and Quality factor . . . . .	62
<b>6</b>	<b>Conclusion and Future Work</b>	<b>65</b>
6.1	Conclusion . . . . .	65

6.2 Future Work . . . . .	65
<b>References</b>	<b>65</b>

## List of Figures

1.1	SPP generation . . . . .	1
1.2	Plasmonic filter proposed by Shiva et al. [1] . . . . .	3
1.3	2 channel demux proposed by Shiva et al [2] . . . . .	3
1.4	Plasmonic sensor proposed by Bahri et al. [3] . . . . .	4
1.5	MIM waveguide topology . . . . .	5
1.6	IMI waveguide topology . . . . .	5
1.7	IMI sensor proposed by Hassan et al. [4] . . . . .	6
1.8	Asymmetrical hybrid sensor proposed by Niu et al. [5] . . . . .	7
1.9	Hybrid waveguide topology . . . . .	7
1.10	Sharmeen et al. [6] . . . . .	8
1.11	Yunping et al. [?] . . . . .	9
1.12	Kong et al. [7] . . . . .	9
1.13	Mahmud et al. [8] . . . . .	9
1.14	Hengli et al. . . . .	11
1.15	Hasan et al. . . . .	12
1.16	Zhao et al. . . . .	12
1.17	Khani et al. . . . .	12
1.18	Wang et al. [9] . . . . .	14
1.19	Liu et al. [2] . . . . .	15
1.20	Shiva et al. [10] . . . . .	15
1.21	Zhao et al. [11] . . . . .	15
3.1	Real part of complex permittivity for Ag . . . . .	25
3.2	Imaginary of complex permittivity for Ag . . . . .	25
3.3	Real part of complex permittivity for Au . . . . .	26
3.4	Imaginary of complex permittivity for Au . . . . .	26
4.1	Resimulation of Chen et al. sensor [12] . . . . .	27
4.2	Representation of the whole Simulation process . . . . .	28
4.3	Geometric structure and mesh view of Chen et al. [12] . . . . .	29
4.4	a) Chen et al.'s result [12] b) Simulated Result . . . . .	29

4.5	$ H_z ^2$ with and without the groove at the resonance wavelength $\lambda = 1392$ nm (a),(c) by Chen et al. [12]and (b),(d) re-simulated work. . . .	30
4.6	(a) Chen et al's [12] Transmission profile b) Re-simulated profile . . .	31
4.7	Demux proposed by Liu et al. [2] . . . . .	31
4.8	a) Resimulated geometric structure b) mesh view . . . . .	32
4.9	a) Liu et al.'s [2] result (b) resimulated result . . . . .	33
4.10	Sensitivity Calculation . . . . .	34
4.11	Figure of merit (FOM) calculation . . . . .	35
4.12	High Q-factor vs Low Q-factor . . . . .	36
4.13	Schematic of a plasmonic waveguide coupled with a ring structure. . .	36
5.1	2D model of the proposed structure . . . . .	39
5.2	a) Transmission spectrum of the system b) Effect of the Baffle and Resonator on system spectrum . . . . .	41
5.3	$ H_z ^2$ field distribution for the presented MIM sensor . . . . .	42
5.4	Initial refractive index variation . . . . .	43
5.5	a) Transmission spectrum for different values of L2 b) Relation between L2 and the resonant wavelengths . . . . .	44
5.6	a)Transmission spectrum for different values of H2 b) Relation between H2 and the resonant wavelengths . . . . .	45
5.7	a)Transmission spectrum for different values of $r_1$ b) Relation between $r_1$ and the resonant wavelengths . . . . .	45
5.8	a)Transmission spectrum for different values of $H_1$ b) Relation between $H_1$ and the resonant wavelengths . . . . .	46
5.9	Finalized Transmission Spectrum . . . . .	47
5.10	Transmission spectrum for different temperatures . . . . .	48
5.11	2D model of the proposed filter . . . . .	48
5.12	2D model of the proposed filter . . . . .	50
5.13	Double ring resonator filter (Filter 1) . . . . .	50
5.14	Initial transmittance curve for filter 1 . . . . .	51
5.15	$ H_z ^2$ field spectrum for filter 1 . . . . .	51
5.16	Transmission spectrum for different values of R1 in filter 1 . . . . .	52
5.17	Double ring resonator filter with stubs (Filter 2) . . . . .	52
5.18	Initial transmittance curve for filter 2 . . . . .	53
5.19	$ H_z ^2$ field spectrum for filter2 . . . . .	53
5.20	Transmission values for different values of L1 of filter 2 . . . . .	54
5.21	triple ring resonator filter (Filter 3) . . . . .	55
5.22	Transmission values for different values of R1 in filter 3 . . . . .	55
5.23	Triple ring resonator filter with stubs (Filter 4) . . . . .	56



5.24	$ H_z ^2$ field distribution for filter 4 . . . . .	57
5.25	Initial transmittance curve for filter 4 . . . . .	57
5.26	Transmission values for different values of L1 in filter 4 . . . . .	58
5.27	2D model of the proposed demultiplexer . . . . .	59
5.28	Transmission spectrum for the two channels . . . . .	61
5.29	$ H_z ^2$ field distribution for port 1 at $\lambda = 865nm$ . . . . .	61
5.30	$ H_z ^2$ field distribution for port 2 $\lambda = 903nm$ . . . . .	62
5.31	Varying the RI from 1 to 1.1 for port 1 . . . . .	63
5.32	Variation of r3 for port 1 . . . . .	63
5.33	Improved channeling and Q-factor . . . . .	64

## List of Tables

3.1	<i>Lorentz-Drude</i> Parameters for Ag [13] . . . . .	25
3.2	<i>Lorentz-Drude</i> Parameters for Au [13] . . . . .	26
4.1	Structural Parameters for Chen et al. [12] . . . . .	28
4.2	Parameters for Liu et al. [2] . . . . .	32
5.1	Structural parameters . . . . .	40
5.2	Final optimized parameters . . . . .	46
5.3	Structural Parameters for the proposed filter . . . . .	49
5.4	Optimized Parameters for finalized filter . . . . .	58
5.5	Structural parameters for demux . . . . .	60
5.6	Improved Q-factor . . . . .	64

## List of Abbreviations

<b>DL</b>	Detection Limit
<b>DMD</b>	Dielectric-Metal-Dielectric
<b>EM</b>	Electromagnetic
<b>FOM</b>	Figure of Merit
<b>FEM</b>	Finite Element Method
<b>LD</b>	Lorentz-Drude
<b>MIM</b>	Metal-Insulator-Metal
<b>RI</b>	Refractive Index
<b>SPP</b>	Surface Plasmon Polariton
<b>TE</b>	Transverse Electric
<b>TM</b>	Transverse Magnetic
<b>QF</b>	Quality Factor

# Acknowledgment

بِسْمِ اللَّهِ الرَّحْمَنِ الرَّحِيمِ

**In the name of Allah, the Most Gracious, The Most Merciful**

First and foremost, we want to thank Allah (SWT), the Most Merciful and Compassionate for His blessings to let us complete this work.

We are grateful to Dr. Rakibul Hasan Sagor, Professor, Department of Electrical and Electronic Engineering, Islamic University of Technology (IUT), for his crucial guidance, support, and recommendations during our studies and research. He provided numerous study possibilities and encouraged us to think beyond the box. We are grateful for all of his knowledge and lessons.

We'd also want to express our gratitude to Infiter Tathfif, Lecturer, Department of Electrical and Electronic Engineering, Islamic University of Technology (IUT), for his unwavering support and guidance during the course of our thesis. We are grateful to him for teaching us the fundamentals of research and equipping us with the necessary knowledge.

We are also grateful for the inspiration and cooperation of the academic members and the brilliant students of the Electrical and Electronic Engineering Department at Islamic University of Technology (IUT).

Finally, we want to express our gratitude to our families for their unwavering mental support throughout the writing of this thesis.

Tahmid Mahbub

Qazi Mahabub-A-Rabbani

Sakib Mahmud

May 2022

## Abstract

Three high-yielding plasmonic refractive index (RI) structures are proposed in this thesis. Those are sensor, demultiplexer and filter. To meet contemporary sensing demands in various industries, such as medical, forensic, and industrial, a sensor consisting of a U-shaped cavity connected with a sub-annular circle was developed. An ultra modern plasmonic 1x2 demultiplexer was made to meet the lackings of conventional demultiplexers such as reduction of bandwidth wastage and minimization of signal delay. The final proposed model of this thesis is a triple ring resonator filter. The optimized filter shows promising results with the minimum possible transmittance. All three structures were constructed using gold as the metal base to ensure minimum oxidation. The wave-solver is COMSOL Multiphysics, which uses the Finite Element Method (FEM) by default. The computational precision of COMSOL Multiphysics is demonstrated through re-simulations of existing structures. Furthermore, the refractive index and the resonant wavelength are linearly related in all three proposed sensors created using the nanoimprint lithography technology. To perceive unknown materials, this linear relationship is used. Furthermore, plasmonic structures' structural properties are susceptible to changes. As a result, the proposed structures are subjected to intensive simulations and optimization processes in order to improve their performance. The proposed sensor was a plasmonic refractive index sensor that had an initial sensitivity of 1320 nm/RIU. After proper optimization, a maximum sensitivity of 3120 nm/RIU was obtained.

The proposed second work with triple ring resonators with rectangular stubs had an initial transmittance dip of 0.062 is observed at the wavelength of 974.7 nm. This result was optimized by adding and varying various structural parameters. The optimized transmission dip obtained is 0.0023 at the wavelength of 912.5 nm which is very low and thus most of the energy is blocked or filtered.

The final structure is a 1×2 channel demultiplexer with concentric ring and nanodisk directly coupled with MIM waveguide. Despite using gold, high quality factor of 22 and 25 were achieved for port 1 and port 2 respectively after intensive optimization. Besides channel spacing of 124 nm was also found. The proposed structures within the book have satisfactory results and is suitable for practical purposes.

# Chapter 1

## Introduction and Background

### 1.1 Surface Plasmon Polariton

Modern optical devices have undergone a huge change over the course of time. Previously, optical devices were limited to run at GHz speed with  $\mu$  m dimensions. With the advent of semiconductor devices, the dimensions were further reduced to nm range, keeping the same operating speed. After that the operating speed was further increased to THz range with the integration of dielectric photonic devices. But using photonic devices has its own set of limitations, being quite bulky and having high cost of implementation. In order to solve this problem, various researchers proposed to implement photonic devices with nm scale dimensions. However it is quite difficult to reduce conventional photonic devices to nm scale because of the diffraction limit of light. Then with the emergence of the Surface Plasmon Polariton (SPP) concept, it was possible to convert the bulky and cumbersome photonic devices to nm dimensions [14].

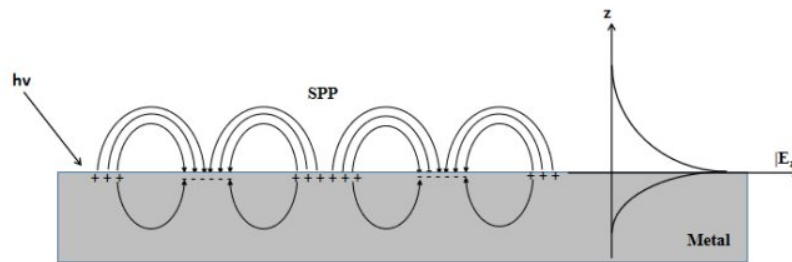


**Figure 1.1:** SPP generation

SPP's are electromagnetic waves that are generated due to the coupling of the incident photon and the surface electron's oscillations (excitations) on the metal-dielectric inter-

face [15]. It is the basic concept based on which various sorts of plasmonic devices are produced. SPPs can freely travel only on the metal dielectric interface, which is quite different from the norm. The amplitude of the excitation continues to decrease with the increasing distance into each medium from the point of incidence, which causes the EM fields to be confined at a sub-wavelength level. The confinement leads to highly enhanced local EM fields and high sensitivity to surface conditions [16].

In Figure 1.1, the SPP propagation on the metal dielectric interface is shown. The decaying property of the EM wave can be understood by exploring the dispersion relation of the wave vector  $k_x$ ,

$$k_x = k_0 \sqrt{\frac{\epsilon_d \epsilon_m}{(\epsilon_d + \epsilon_m)}}. \quad (1.1)$$

Where,

$k_0 = \frac{\omega}{c}$  represents the free space wave vector.

SPP's can be useful in multiple fields due to its lucrative high operating speed and small dimension. It can be applied in sub-wavelength optics, near-field optics, data storage purposes, various sensing fields (bio sensing, chemical sensing) etc. [14]. As the performance of the plasmonic devices are noteworthy, SPP's can be used to develop devices like sensors, filters and demultiplexers.

## 1.2 Plasmonic Devices

### 1.2.1 Plasmonic Filter

Plasmonic filters are one of the more attractive research topics within recent years. More and more research is being pooled in it to effectively produce devices which can give performance similar to the traditional filters or even better compared to them. Filters are basically filtering (controlling the flow) the signal within a certain frequency range. Most of the research done on this consists of two types of filters, band pass filters and band stop filters. Band pass filter, like the conventional one, passes the signal within a range of frequencies and cancels the signal when it is out of the range. One of the proposed filter is depicted below:

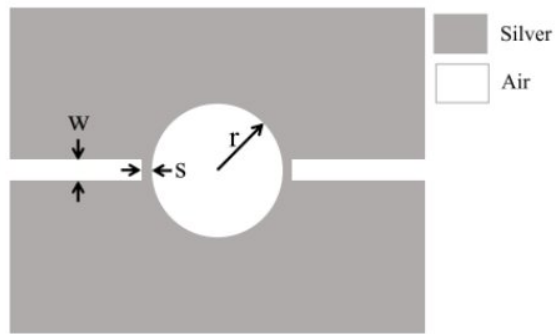


**Figure 1.2:** Plasmonic filter proposed by Shiva et al. [1]

On the other hand band stop filters cut off the signal at a certain band of frequencies. Different applications require either of the two filters. Like planar spoof of transmission lines require bandpass filters and band stop filters for faster approach [17]. Different resonators are proposed for faster procession in MIM filter arrangement like nano disc, square ring, circular ring etc.

### 1.2.2 Plasmonic Demultiplexers

Plasmonic demultiplexers, like the filters described above, is one of the recent interests within the field of optical devices. Conventional demultiplexer represents one to many channel demultiplexing like  $1 \times 2$  demultiplexer,  $1 \times 8$  demultiplexer etc. But the conventional demultiplexer faces trouble in the form of bandwidth wastage and signal delay. Keeping this in mind, various researchers have proposed in developing plasmonic demultiplexers, that will not suffer from bandwidth wastage and try to minimize the signal delay as much as possible. One of the proposed demultiplexers is depicted below [2],

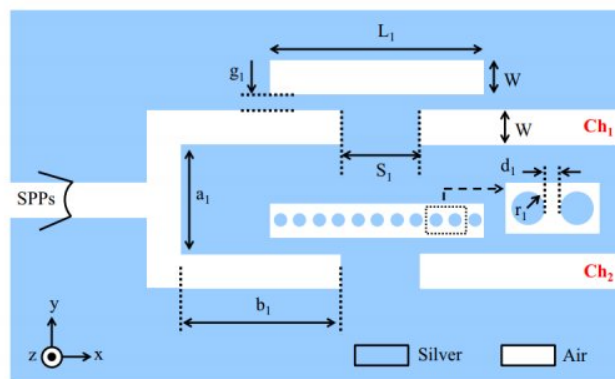


**Figure 1.3:** 2 channel demux proposed by Shiva et al [2]



### 1.2.3 Plasmonic Sensor

Plasmonic sensors, otherwise known as, refractive index (RI) sensors, quantifies the environment quantities in terms of change of refractive index and can help identify the current state of the observed object. Here, mainly change of refractive index is observed. So the device should be sensitive enough to observe the change in refractive index due to the impact of the surroundings. As RI sensors depict the state of the environment, it can be used for different applications like temperature sensing [18], bio sensing [19], pressure sensing [20] etc. One of the proposed sensors is shown below [3],

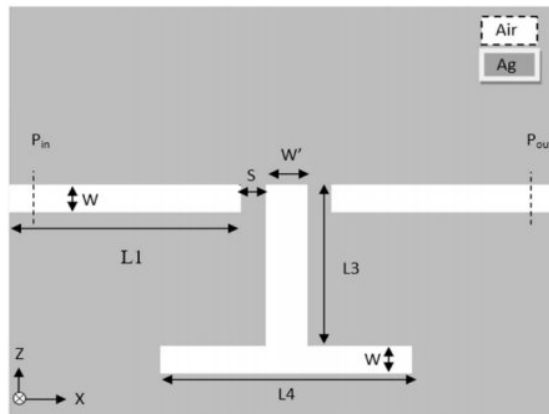


Figure 1.4: Plasmonic sensor proposed by Bahri et al. [3]

## 1.3 Waveguide topology

Devices are designed according to different topologies to give better results according to different shapes and have different advantages. Based on these, the waveguide topologies can be divided into three categories. These are :

- MIM waveguide topology
- IMI waveguide topology
- Hybrid topology

### 1.3.1 MIM waveguide

Metal-Insulator-Metal waveguide topology is perhaps the most commonly used topology in all optical devices. It's structural configuration is depicted below,

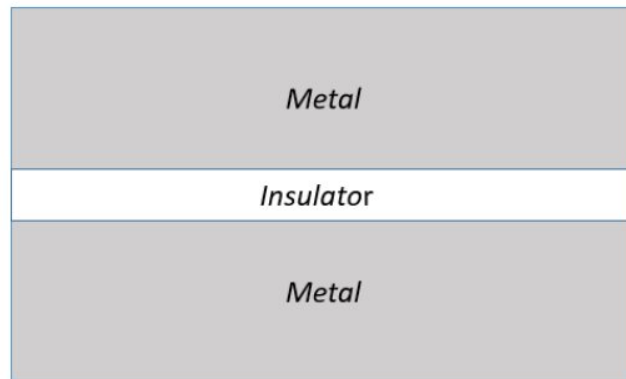


**Figure 1.5:** MIM waveguide topology

As we can see from the above figure, the insulating layer is sandwiched between two metallic layers. The MIM layers is mainly preferred among the researchers due to it's strong confinement ability. As it was stated previously, that due to high confinement ability, it increases the sensitivity of the device and has high transmission speed. But it mainly faces the issue of lower propagation length compared to other types of topologies. Due to the propagation length being quite low, it has comparatively less propagation loss. This low propagation loss is the main cause behind the high interest in manufacturing photonic devices using MIM structures.

### 1.3.2 IMI waveguide

This topology is quite different from the above mentioned MIM topology as it requires the metal layer to be sandwiched between the insulating layers, instead of the previous type of structure.

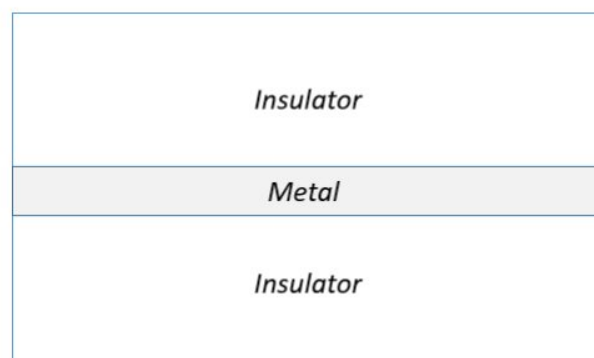


**Figure 1.6:** IMI waveguide topology

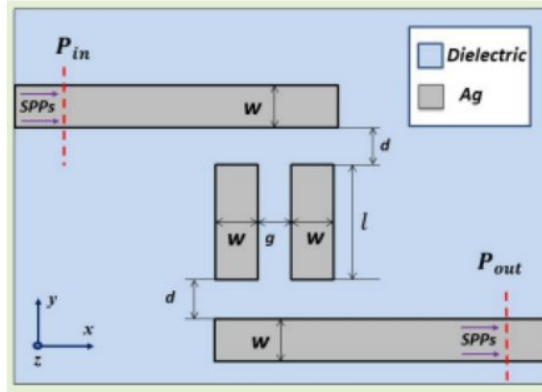


**Figure 1.7:** IMI sensor proposed by Hassan et al. [4]

The IMI waveguide topology has different characteristics than the MIM waveguide. Its main advantage lies in its ability to generate plasmons with high propagation length. Due to this high propagation length of wave transmission, it can be used in optical devices which operate on high distances. The IMI waveguide structure is also known as Long range Surface Plasmon (LRSP) [21]. The main reason behind this long propagation length is discussed by Hassan et al, where he stated that the field line distribution causes less attenuation and larger propagation length. Though the structure has a large propagation length, it suffers from very poor confinement ability. Due to this it is cumbersome to produce highly sensitive structures using IMI waveguide topology.

### 1.3.3 Hybrid waveguide

As it can be observed from the two waveguide topologies described above, MIM structure has confining ability but lower propagation length, while IMI waveguides have higher propagation. So in order to produce a device which will not only have high confinement and good output, but will also have high propagation constant, hybrid waveguides are proposed. The structure of a hybrid waveguide is depicted below,

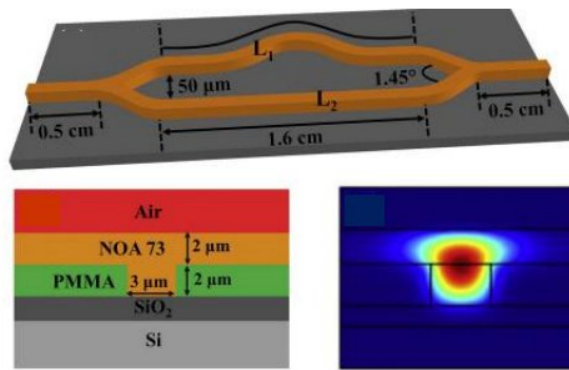


**Figure 1.8:** Asymmetrical hybrid sensor proposed by Niu et al. [5]



**Figure 1.9:** Hybrid waveguide topology

As we can see from fig 1.9 this waveguide topology consists of two different dielectric medium plastered along with a metal surface. The dielectric medium with lower refractive index is kept in the middle between the other dielectric medium and the metallic surface. As the two dielectric mediums are different, there is a strong coupling the lower surface and the upper surface, which allows higher confinement. Also the medium doesn't consist of double metallic layer. So there is less chance of the propagation length being shortened due to interference [22]. As the waveguide provides both the advantages of the above mentioned topologies, it is increasingly becoming a lucrative topic to research on which will enhance the optical field further.

## 1.4 Literature Review

Photonic devices have been a great interest of research due to its ability to transfer datas with high operating speed. The transfer speed along with low attenuation of signal, gives the devices more stability in terms of signal generation and transfer, compared to conventional devices. Furthermore, fabrication of the devices are much easier with modern technology as nanometer scale designing is being developed rapidly [23].

Numerous devices have been developed to produce smart and lightweight devices which can easily replace the conventional ones. Nanosensors have been extensively researched on, in order to produce lightweight devices so that they can easily and uniquely sense the observed specimen. The main reason behind doing such an extensive result can mainly be attributed to the fact that using PCF cables, highly sensitive sensors can be generated easily [24, 25]. So, the main target in developing nano plasmonic sensors is to develop novel structures which will have high sensitivity.

In 2019, Yunping et al. proposed an MIM waveguide based plasmonic sensor consisting of a double sided nanodisk and two rectangular slots as resonant cavities [?]. The sensitivity and FOM was found to be around 750 nm/ RIU and 99 respectively. Coupling between multiple ring cavity and the waveguide based MIM sensor was proposed by Sharmeen et al, with the sensitivity and FOM being 3573 nm/RIU and 21.9 respectively [6]. The author also proposed that the device can be used to detect gasses.

Kong et al. proposed a RI sensor which can also be used as a temperature sensor, where Refractive index sensitivity and temperature sensitivity of the proposed structure is  $3.38 \times 10^6$  % /RIU and 82% /K respectively [7].

Mahmud et al. proposed a pentagonal shaped cavity based highly sensitive sensor with sensitivity and FOM being around 2325 nm/RIU and 46 respectively [8].

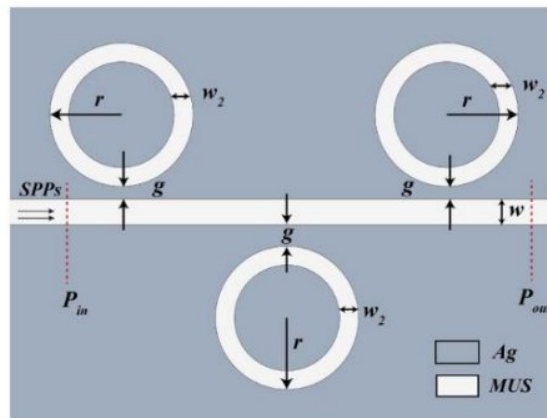


Figure 1.10: Sharmeen et al. [6]

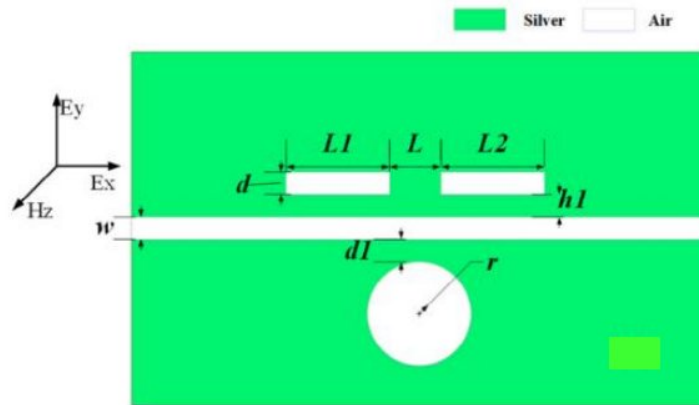


Figure 1.11: Yunping et al. [?]

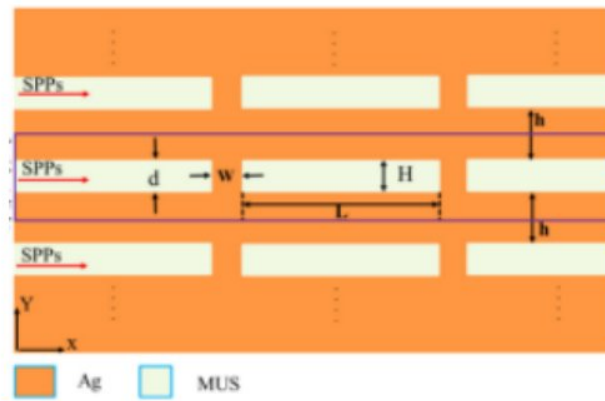


Figure 1.12: Kong et al. [7]

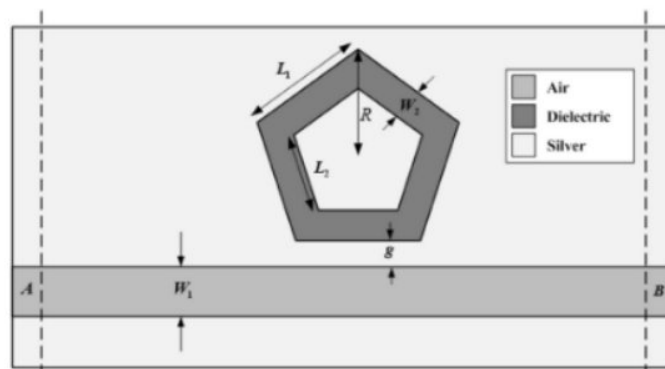


Figure 1.13: Mahmud et al. [8]

Now models proposed by [26–40] are compared among each other in Table 1.1

Ref.	Year	Topology	Material used	Model	S (nm/RIU)	FOM
[21]	2020	Circular Ring	Ag	Drude	1295	159.6
[22]	2019	Square Ring	Ag	Drude-Lorentz	1367	25
[23]	2018	Square Ring	Ag	Drude-Lorentz	1200	19.7
[24]	2018	Coupling between two stubs & one ring	Ag	Debye-Drude	1268	280
[25]	2017	Asymmetric MIM structure	Ag	Debye-Drude	718	4354
[26]	2016	Rectangular cavity along with two slot cavities	Ag	Drude	800	13500
[27]	2020	Dumbbell shaped cavity directly coupled with two rectangular stubs	Ag	Drude	1260	120
[28]	2015	Slot cavity above or below a groove cavity	Ag	—	1131	$1.6 \times (10^7)$
[29]	2017	Rectangular cavity coupled with a Waveguide consisting of a baffle	Ag	—	1400	17500
[30]	2020	Two consecutive disk resonators	Ag	Drude	1500	242.66
[31]	2019	Nanocubes	Au	Drude	1002	417
[32]	2020	Nano-array with rhombus particles	Au	Drude	1006	305.7
[33]	2021	Asymmetric ring cavity	Au	—	440.2	52.6
[34]	2021	Mach Zehnder Interferometer	Au	Drude	989.6	—
[35]	2019	Asymmetric dual side-coupled U shaped cavities	Au	Drude	496	—

**Table 1.1:** Comparison between recent RI sensors.

Now that some of the recent proposed sensors have been reviewed, we will focus on some other plasmonic devices like filters and demultiplexers.

Filters and demultiplexers are some of the recent growing interests within the plasmonic research community. The opportunity to convert bulky and cumbersome devices

to lightweight contemporaries is the main basis for this increase.

As filters cut off signals based on its characteristic (pass or stop), research is being done to produce filters which have very high transmission peaks / dips and cover a sufficient bandwidth. If the bandwidth is too large, it might fail to act as a proper filter. Based on this, more precedence is given to the quality factor for measuring the performance of the filter.

Some research related to filters have been reviewed. Hengli et al. in 2021 proposed a Silver based plasmonic filter with transmission peaks 528 nm and 815 nm respectively [41]. In 2020, Hassan et.al proposed a rectangular nano-resonator as an optical filter using Ag and obtained a Q-factor of 16.8 [42]. Zhao et.al in 2011 proposed a nano plasmonic optical switch based on  $Ga - Si_3N_4 - Ga$  waveguide which had a Q-factor of 20.1 [43]. A comparison table between some recently proposed filters is given in Table 1.2

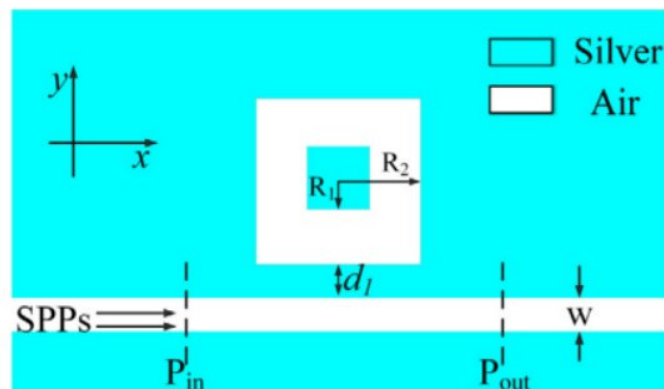


Figure 1.14: Hengli et al.



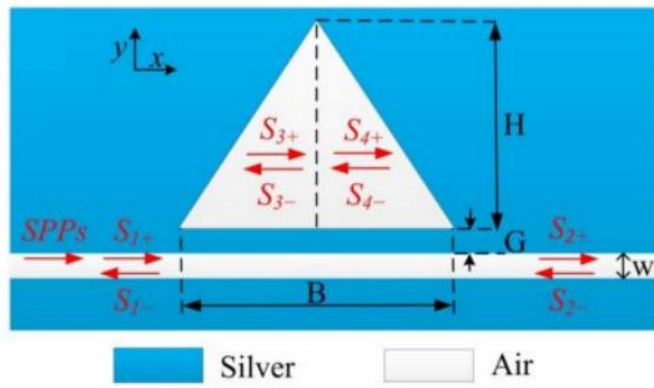


Figure 1.15: Hasan et al.

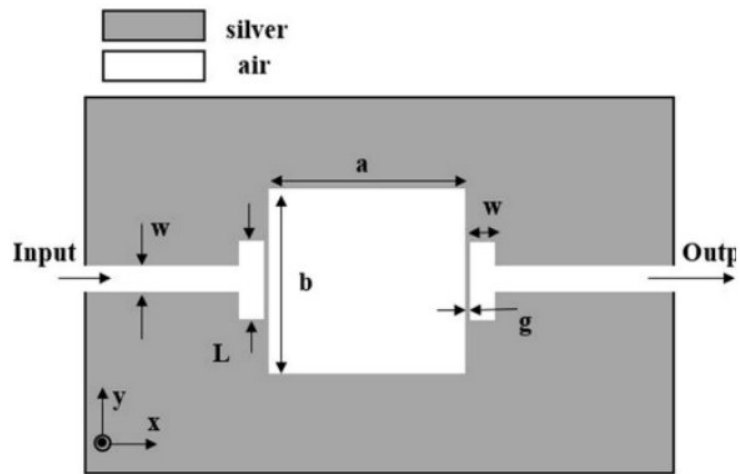


Figure 1.16: Zhao et al.

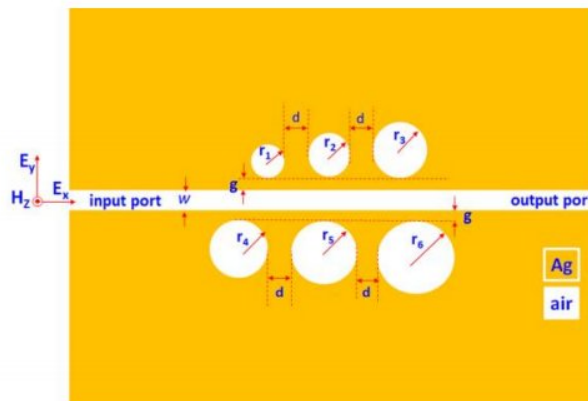


Figure 1.17: Khani et al.

Now filter models proposed by [42,44–54] are compared among each other in Table 1.2

Ref.	Year	Topology	Material used	Model	Q-factor	Transmission Peaks/Dips
[39]	2018	Circle nanodisk	Ag	Drude-Lorentz	26.2	0.35
[40]	2012	Rectangular nanodisk	Ag	Lorentz-Drude	–	0.72
[41]	2016	Nanorods in hexagonal	Ag	Lorentz-Drude	55	0.59,0.34,0.23
[37]	2020	Rectangular nanodisk	Ag	Lorentz-Drude	6.4, 16.8	0.72, 0.54
[42]	2019	Square nanodisk	Ag	Drude	–	0.84,0.78, 0.92
[43]	2013	Rectangle cavity	Ag	Lorentz-Drude	–	0.08
[44]	2010	Nanonotch structure	Ag	Drude-Lorentzian	–	0.05
[45]	2018	Hexagonal & rotating ellipse	Ag	Drude	–	0.009
[46]	2009	Directional coupler	Ag	Drude	–	0.03
[47]	2021	Color filter	Ag	Drude	349	–
[48]	2021	Equilateral triangle	Ag	Johnson and Christy	322	–
[49]	2022	T-waveguide, square resonator cavity	Ag	Johnson and Christy	91	0.99

**Table 1.2** Comparison of recent filters.

Demultiplexers have the same features as filters. But here instead of having 1 channel input and 1 channel output, demuxes have single input channel and multiple output channels. Demultiplexers having multiple channels can act as a switch for certain wavelengths. As the demultiplexer focus on inhibiting some signal at some wavelength range and allowing flow of signal at some other wavelength, quality factor is also highly preferred as the performance index of the demultiplexing devices.

In 2011, Wang et al. [9] proposed a tunable nanodisk resonator based demultiplexer which could change the demultiplexing wavelength based on the number of resonators used. The material used for the designing is silver (Ag) and the highest transmission achieved is 70%.

A T-shaped demux with nanodisks proposed by Liu et al. [2] shows 2 channel demultiplexing. By changing the radius of the disks, a separation of 8nm between the two wavelengths is shown.

Khani et al. [10] demonstrated a 2,4,6 channel demux using rectangular resonators incorporating nanorods within them. The change in the number of nanorods in the resonators provided the shifting of the wavelengths.

Based on square resonators, Zhao et al [11] came up with a demux design which can be used for  $1 \times N$  channels. The lowest FWHM measured was to be 10nm. Cascading the square resonators provided the shift in channel wavelengths.

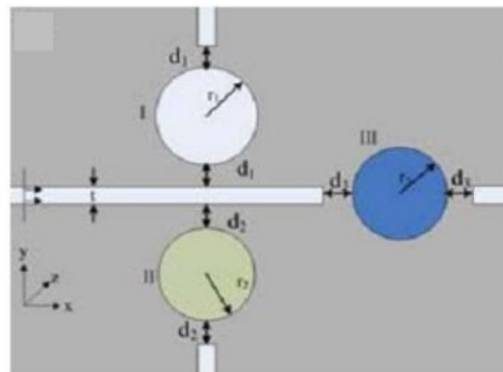


**Figure 1.18:** Wang et al. [9]

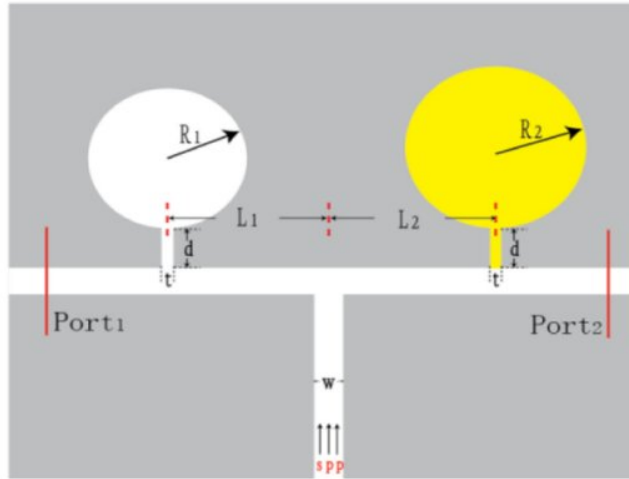


Figure 1.19: Liu et al. [2]

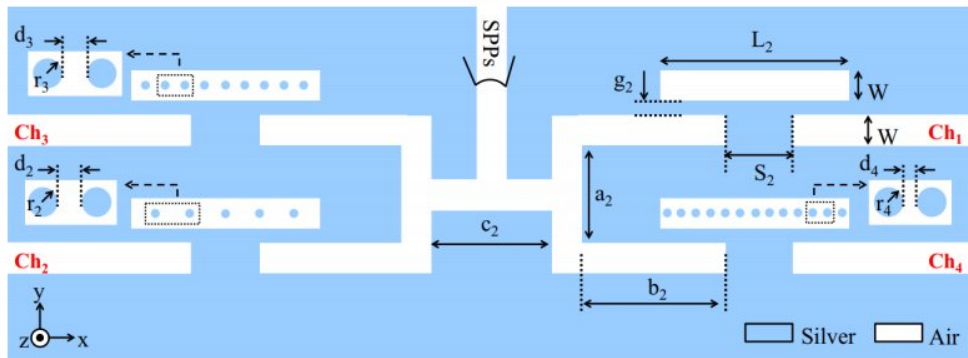


Figure 1.20: Shiva et al. [10]

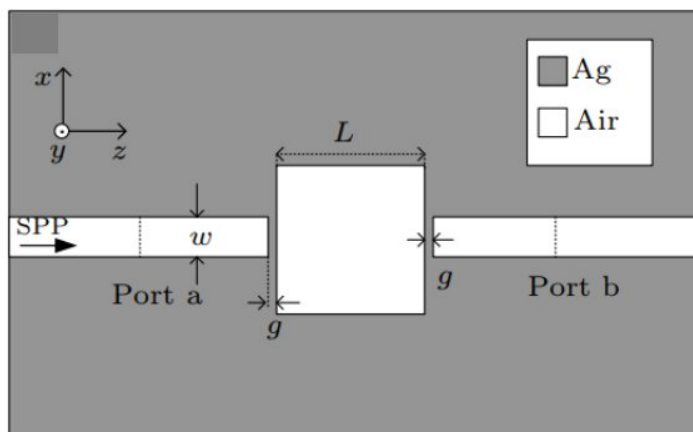


Figure 1.21: Zhao et al. [11]

## 1.5 Thesis Objective

If the literature review is analyzed, it can be seen that there is an abundance of research done on silver (Ag) related photonic devices. This can be mainly attributed to the fact that Ag is a highly sensitive metal and highly effective devices can be produced easily with better results compared to using other metals. But using Ag as a metallic base has its own share of issues. As Ag is a highly reactive metal, it is prone to oxidation within a certain period. So it has a very low longevity compared to using other metals. The main objective of this thesis is to produce some devices which will not only give highly improved results but also higher longevity. To fulfill this objective, it has been decided to use gold (Au) as the metallic base. Gold is very less reactive compared to Ag and thus will have higher longevity.

Furthermore, with this thesis, it is desired to propose devices which can be utilized in multiple fields like bio sensing, thermal sensing, filtering and demultiplexing.

The performance indices of each device has to be optimized through trial and error to produce plasmonic devices with the best results.

## 1.6 Thesis Layout

Chapter 1 presents a brief introduction to how SPP works and its fundamental role in producing various plasmonic devices. Along with that, many plasmonic devices were introduced and the waveguide topologies that can be used for each device were briefly discussed. Recent sensor, filters and demultiplexers were compared against each other in the Literature review section.

Chapter 2 presents the various equations based on which the whole structure is developed. Maxwell's equation, constitutive equation and FEM were studied to get a sense on how the plasmonic interaction takes place.

Chapter 3 introduces the methods with which various researchers modeled materials like Ag, Au for their research purpose. The complex dielectric relationship of the two materials are compared against each other.

Chapter 4 describes the theory related to ring resonators. Performance indices related to plasmonic devices have been briefly discussed. Resimulation of previous studies were done to check the validity of the simulation setup.

Chapter 5 describes three new plasmonic devices eg . a sensor, a filter and a demultiplexer based on MIM waveguide topology. The parameters were extensively optimized to give optimal performance. Various application related to sensing were further researched on this chapter.

Chapter 6 concludes the thesis, by giving a brief summary of the whole paper and giv-

ing insight onto the future works that can be progressed.

# Chapter 2

## Electromagnetic Wave Theory

### 2.1 Maxwell's and Wave equations

#### 2.1.1 Maxwell's equations

The Maxwell's equations are a set of differential and integral equations that describe the connections between basic electromagnetic quantities. For electromagnetic analysis, Maxwell's equations must be solved. The equations are given in differential form and can be accommodated by Finite Element Method (FEM). Maxwell's equations can be represented in terms of generic time-varying fields as,

$$\text{Ampere - Maxwell Law} : \nabla \times H = J + \frac{\partial D}{\partial t} \quad (2.1)$$

$$\text{Faraday's Law} : \nabla \times E = -\frac{\partial B}{\partial t} \quad (2.2)$$

$$\text{Gauss Law} = \nabla \cdot D = \rho \quad (2.3)$$

$$\text{Gauss Law for magnetism} = \nabla \cdot B = 0 \quad (2.4)$$

where,

E = Electric field intensity,

D = Electric flux density

H = Magnetic field intensity,

B = Magnetic flux density,

J = Current density,

$\rho$  = Electric charge density

In Electromagnetic (EM) Wave, there is another rudimentary equation known as *the continuity equation*,

$$\nabla \cdot J = -\frac{\partial \rho}{\partial t} \quad (2.5)$$

### 2.1.2 Constitutive equation

Maxwell's equations describe the fields created by charge and current without defining how they are generated. Constitutive equations describe the nature of matter in contact with fields and allow *Maxwell's equations* to be applied to new situations. The following are examples of constitutive equations:

$$D = \epsilon_0 E + P, \quad (2.6)$$

$$B = \mu_0(H + M), \quad (2.7)$$

$$J = \sigma E, \quad (2.8)$$

where,

$\epsilon_0$ =Electric permittivity of vacuum, ( $Fm^{-1}$ ),

$\mu_0$ =Magnetic permeability of vacuum, ( $Hm^{-1}$ ),

$\sigma$ = Electric Conductivity, ( $Sm^{-1}$ ).

Considering the *EM* wave propagation in vacuum media, the numerical value of the permittivity and permeability is,

$$\mu_0 = 4\pi \times 10^{-7} Hm^{-1},$$

$$\epsilon_0 = \frac{1}{c_0^2 \mu_0^2} = 8.854 \times 10^{-12} Fm^{-1}.$$

Where,  $\mathbf{P}$  stands for dielectric polarization of the material under the influence of an external electric field. It is described as a dipole moment in unit volume cell and linearly related to the applied *E*-field, dielectric constant ( $\epsilon_0$ ), and the medium's susceptibility ( $\chi_e$ ). Hence,

$$P = \epsilon_0 \chi_e E. \quad (2.9)$$

Similarly,  $\mathbf{M}$  denotes the magnetization vector with the presence of external *H*-field. which describes the permanent or temporary magnetic dipole moments in a magnetic material.  $\mathbf{M}$  also describe the density of magnetic dipole vector and proportionally



related to applied  $H$ -field, permeability ( $\mu_0$ ) and magnetic susceptibility ( $\chi_m$ ) of the medium. Hence,

$$M = \mu_0 \chi_m H. \quad (2.10)$$

For linear materials, which have constant material properties with the variation of applied field, the constitutive equation can be described as,

$$D = \varepsilon_0(1 + \chi_e)E = \varepsilon_0 \varepsilon_r E = \varepsilon E, \quad (2.11)$$

$$B = \mu_0(1 + \chi_m)H = \mu_0 \mu_r H = \mu H, \quad (2.12)$$

where,

$$\varepsilon_r = (1 + \chi_e),$$

$$\mu_r = (1 + \chi_m).$$

### 2.1.3 Generalized Constitutive Equations (Non-Linear Materials)

For non-linear materials, there can exist polarization and magnetization without the presence of an external electric  $E$ -field and magnetic  $H$ -field. So, an additional term to address the non-zero effect is added with the constitutive equation. Constitutive relation for  $E$ -field is,

$$D = \varepsilon_0 \varepsilon_r E + D_r. \quad (2.13)$$

Here,  $D_r$  = Electric flux density without the  $E$ -field, known as *remanent electric flux density*.

Constitutive relation for  $H$ -field is,

$$B = \mu_0 \mu_r H + B_r. \quad (2.14)$$

Here,  $B_r$  denotes the magnetic flux density with the absence of  $H$ -field known as *remanent magnetic flux density*.

Now the current density expressed in eqn[8] can be written by adding an externally generated current  $J^e$  to the constitutive equation. This can be expressed as,

$$J = \sigma E + J^e \quad (2.15)$$

### 2.1.4 Wave Equation

The wave equation is the most essential aspect and governing equation in the propagation of EM waves. It has been proved that Maxwell's equation can be used to get the EM wave equation (electric). Equation (2.2) is multiplied by  $\nabla$  to give the following result:

$$\nabla \times (\nabla \times E) = \nabla \times \left( -\frac{\partial B}{\partial t} \right) = -\frac{\partial}{\partial t} (\nabla \times B) \quad (2.16)$$

Now, by evaluation of eq. (2.1), eq. (2.11), and eq. (2.12),

$$\nabla \times (\nabla \times E) = -\mu \varepsilon \frac{\partial^2 E}{\partial t^2} \quad (2.17)$$

Again, considering  $\frac{\partial}{\partial t} = j\omega$ ,  $\varepsilon = \varepsilon_0 \varepsilon_r$ , and  $\mu = \mu_0 \mu_r$ , this equation becomes,

$$\nabla \times (\mu_r^{-1} \nabla \times E) - k_0^2 \varepsilon_r E = 0, \quad (2.18)$$

where,  $k_0$  is the wave number of free space and is defined as,

$$k_0 = \omega \sqrt{\mu_0 \varepsilon_0} = \frac{\omega}{c_0} \quad (2.19)$$

Now, using the relation  $\varepsilon_r = \eta^2$  for the linear materials where  $\eta$  is the refractive index and assuming  $\mu_r = 1$ , the equation can be re-written as,

$$\nabla \times (\nabla \times E) - k_0^2 \eta^2 E = 0 \quad (2.20)$$

## 2.2 Simulation Modeling

### 2.2.1 Finite Element Method

The finite element method (*FEM*) is more successful at solving issues involving complicated geometry and inhomogeneous medium than other mathematical approaches that are conceptually simpler and easier to code, such as the finite difference method (*FIT*) and the method of moments (*MOM*). *Maxwell's* equation is used to compute electromagnetic fields. The magnetic potential vector  $A$  and the electrical voltage  $V$  are written as,

$$B = \nabla \times A, \quad (2.21)$$

$$E = -\nabla \times V, \quad (2.22)$$

eq[2] can be now written as,

$$\nabla \times E = -\nabla \times \left( \frac{\partial A}{\partial t} \right) \quad (2.23)$$

As the electric field potential for the non-static fields is increased with an induced voltage,

$$E = -\nabla V - \left( \frac{\partial A}{\partial t} \right) \quad (2.24)$$

Conductors replace the term charge density with Dirichlet type boundary equation. The potential equation reduces to a *Laplace equation*,

$$\nabla \cdot (\varepsilon \nabla V) = 0, \quad (2.25)$$

here,  $\varepsilon$  denotes a diagonal tensor, neglecting the off-diagonal coupling terms:

$$\varepsilon = \begin{bmatrix} \varepsilon_x & 0 & 0 \\ 0 & \varepsilon_y & 0 \\ 0 & 0 & \varepsilon_z \end{bmatrix} \quad (2.26)$$

The electric field energy is expressed as,

$$W_E = \int_V \frac{D \cdot E}{2} dV = \int_V \frac{\varepsilon |E|^2}{2} dV \quad (2.27)$$

Scattering parameters can be evaluated using the equation,

$$S_{ij} = \frac{\int_{port_i} (E_j \cdot E_i^*) dA_i}{\int_{port_i} (E_j \cdot E_j^*) dA_i}, \quad (2.28)$$

The time average reflection and transmittance coefficient,  $T$  is obtained by,

$$T = |S_{ij}|^2 \quad (2.29)$$

# Chapter 3

## Plasmonic Materials

### 3.1 Refractive Index and Complex Permittivity

Analysts are always investigating the many features of plasmonic materials. Permittivity and permeability are two complex dielectric functions that define plasmonic materials. Because the magnetic field,  $\mu$  has a weak impact on metals, is regarded as unity. As a result, a plasmonic material's complicated permittivity can be written as:

$$\varepsilon(\omega) = \varepsilon_1(\omega) - i\varepsilon_2(\omega), \quad (3.1)$$

where,  $\varepsilon_1(\omega)$  = real part of  $\varepsilon(\omega)$ , which accounts for polarization. A negative  $\varepsilon_1(\omega)$  indicates a superior plasmonic nature, and  $\varepsilon_2(\omega)$  = imaginary part of  $\varepsilon(\omega)$ , which accounts for SPP propagation loss. A lossy system is represented as a rising  $\varepsilon_1(\omega)$ .

The complex refractive index is now written as,

$$\eta = \eta_1 - i\kappa, \quad (3.2)$$

where,

$\eta_1$  = refractive index, and

$\kappa$  = extinction coefficient.

Since the refractive index and the permittivity are interrelated, thus

$$\eta_1 = \frac{1}{\sqrt{2}} \times \sqrt{(\sqrt{(\varepsilon_1^2 + \varepsilon_2^2)} + \varepsilon_1)}, \quad (3.3)$$

$$\kappa = \frac{1}{\sqrt{2}} \times \sqrt{(\sqrt{(\varepsilon_1^2 + \varepsilon_2^2)} - \varepsilon_1)} \quad (3.4)$$

## 3.2 Material Modeling

Rakic et al. conducted research on eleven prospective plasmonic materials in 1998 and calculated the numbers required to suit two well-known models for material modeling at high optical frequencies: *Lorentz-Drude* and *Drude* [13].

### 3.2.1 Drude Model

The complex permittivity equation is primarily influenced by two factors: *free-electron effects/intraband effects* and *bound-electron effects/interband effects*, according to several studies. The intraband effects can be characterized as follows using the *Drude* model:

$$\varepsilon_{free}(\omega) = 1 - \frac{\omega_p^2}{(\omega^2 - i\omega\Gamma_0)}, \quad (3.5)$$

where,  $\omega_p$  and  $\Gamma_0$  correspondingly denote the plasma frequency and collision frequency.

### 3.2.2 Lorentz Model

The *Lorentz* model can also be used to express interband effects as follows:

$$\varepsilon_{bound}(\omega) = \sum_{i=1}^m \gamma_i \omega_i^2 / (\omega_i^2 - \omega^2 + i\omega\Gamma_i), \quad (3.6)$$

where,  $\omega_i$ ,  $\gamma_i$ , and  $\Gamma_i$  denote the resonant frequency, oscillator strength and damping frequency, respectively.

### 3.2.3 Lorentz-Drude Model

The Lorentz-Drude Model is equal to the sum of equations (5) and (6).

$$\varepsilon(\omega) = \varepsilon_{free}(\omega) + \varepsilon_{bound}(\omega) \quad (3.7)$$

The real and imaginary parts of complex permittivity and complex refractive index of two materials (Ag, Au) are calculated numerically and shown using the *Lorentz-Drude* model in the following section.

## 3.3 Ag Modeling

The *Lorentz-Drude* parameters for Ag are listed in table 3.1

Parameters	Values (eV)
Plasma frequency ( $\omega_p$ )	9.01
Collision frequency ( $\Gamma_0$ )	0.048
Oscillator strength ( $\gamma_i$ )	[0.845; 0.065; 0.124; 0.011; 0.840; 5.646]
Damping frequency ( $\Gamma_i$ )	[0.048; 3.886; 0.452; 0.065; 0.916; 2.419]
Resonant frequency ( $\omega_i$ )	[0; 0.816; 4.481; 8.185; 9.083; 20.29]

**Table 3.1:** Lorentz-Drude Parameters for Ag [13]

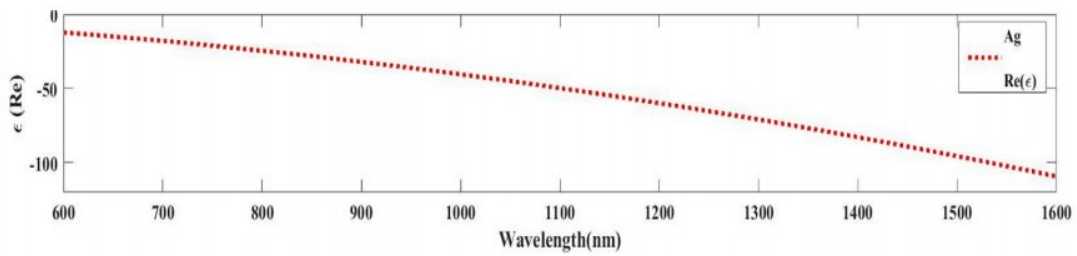


**Figure 3.1:** Real part of complex permittivity for Ag

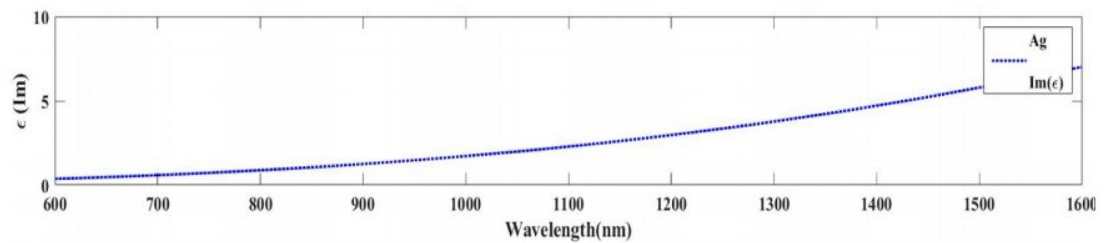


**Figure 3.2:** Imaginary part of complex permittivity for Ag

### 3.4 Au Modeling

The *Lorentz-Drude* parameters for Au are listed in table 3.2

Parameters	Values (eV)
Plasma frequency ( $\omega_p$ )	9.03
Collision frequency ( $\Gamma_0$ )	0.053
Oscillator strength ( $\gamma_i$ )	[0.760; 0.024; 0.010; 0.071; 0.601; 4.384]
Damping frequency ( $\Gamma_i$ )	[0.053; 0.241; 0.345; 0.870; 2.494; 2.214]
Resonant frequency ( $\omega_i$ )	[0; 0.415; 0.830; 2.969; 4.304; 13.32]

**Table 3.2:** *Lorentz-Drude* Parameters for Au [13]

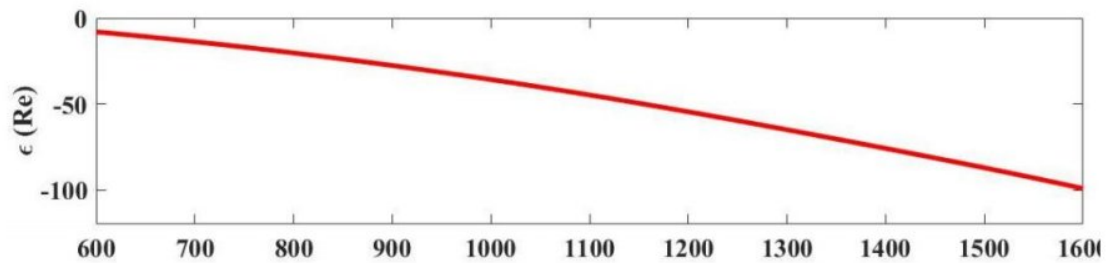


**Figure 3.3:** Real part of complex permittivity for Au

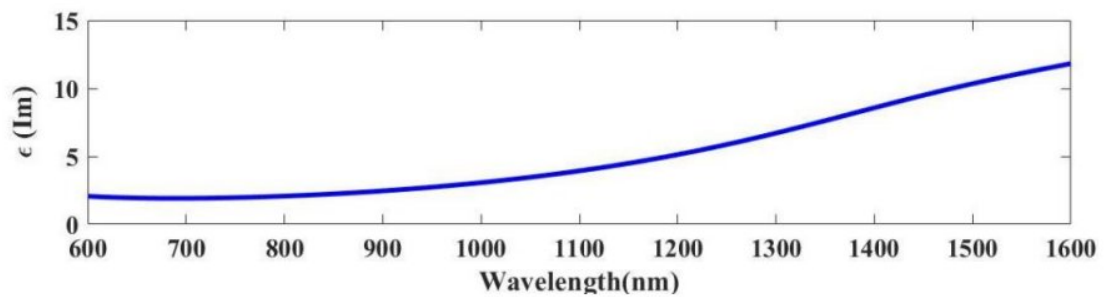


**Figure 3.4:** Imaginary of complex permittivity for Au

# Chapter 4

## Resimulation and Performance Metrics

### 4.1 Resimulation for Quality validation

The simulation setup must be validated before designing our own models. So the resimulation of some published papers are verified in this section. For achieving this, papers related to sensor, demultiplexer and filter were resimulated in this section.

#### 4.1.1 Resimulation of Sensor

“A Refractive Index Nanosensor Based on Fano Resonance in the Plasmonic Waveguide System” proposed by Chen et al. [12], published in “*IEEE Photonics Technology Letters*” is resimulated in this section. Figure 4.4 exhibits the structure of the proposed sensor and Table-4.1 contains the geometric parameters of the structure.

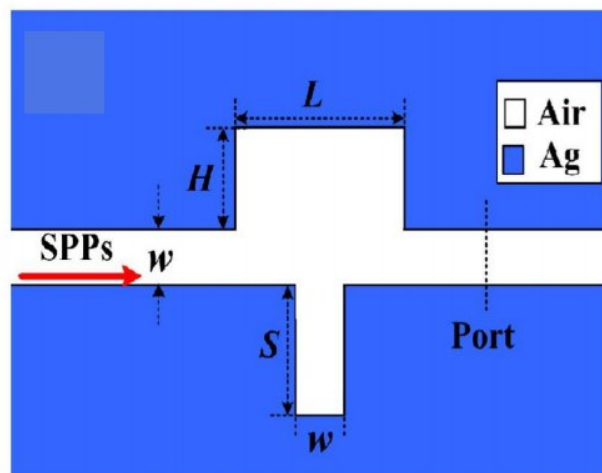
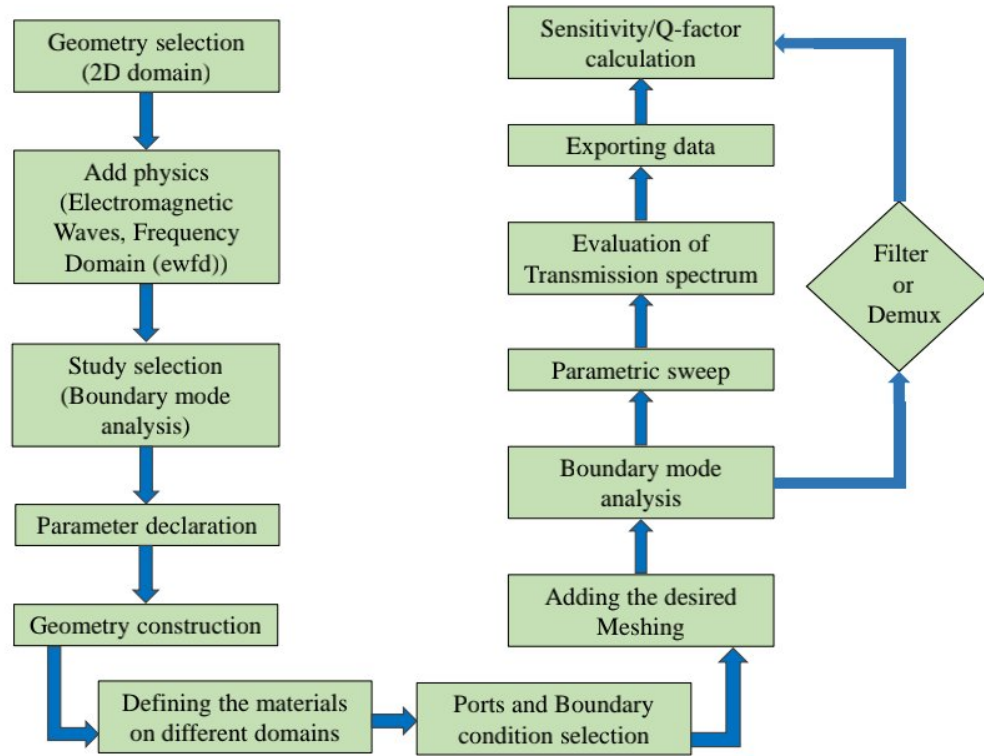


Figure 4.1: Resimulation of Chen et al. sensor [12]



Parameters	Denoted Symbols	Value	Unit
Length of the groove	L	200	nm
Height of the groove	H	225	nm
Length of the stub	S	225	nm
Width of stub and waveguide	w	50	nm

**Table 4.1:** Structural Parameters for Chen et al. [12]



**Figure 4.2:** Representation of the whole Simulation process

As it can be observed from fig 4.2 that the process consists of several steps. At first, 2D geometry domain and Electromagnetic Waves physics are chosen. The geometry is then created with appropriate parameters. Subsequently, plasmonic materials, ports, and boundary conditions are assigned to the structure. The material in both the resonator cavities is Air which has a refractive index (RI) value of  $n = 1$ .

Afterwards, extra fine meshing is applied for the better accuracy of the result. Figure 4.3 shows the geometry construction and the meshed structure respectively using

COMSOL Multiphysics software.

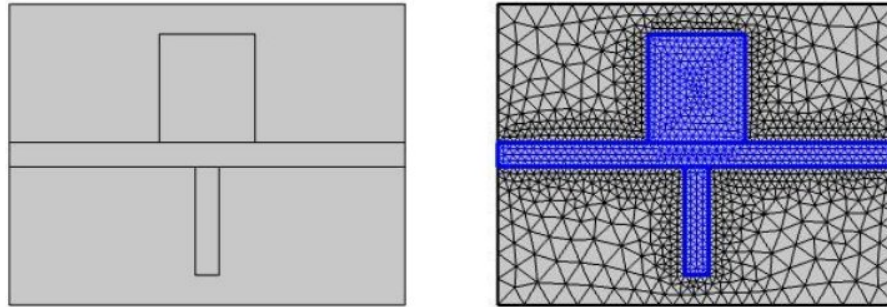


**Figure 4.3:** Geometric structure and mesh view of Chen et al. [12]

After that parametric sweep is utilized to observe the effect of variation of various parameters on the simulation. As sensitivity is the preferred performance index for a sensor, it was calculated after exporting the simulated data .

The transmission spectrum of the original work and re-simulated work is depicted in Fig 4.4 [a,b] respectively. The spectrum was simulated for a refractive index of  $n = 1$ . Along with that the illustrated fields are compared in Fig 4.5 [a-d]. Here the fields were observed for the structure containing groove one time and the other time without groove.

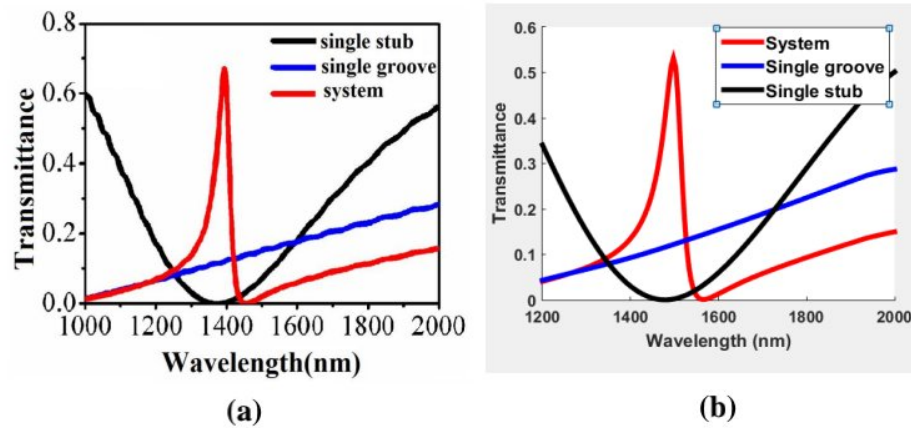


**Figure 4.4:** a) Chen et al.'s result [12] b) Simulated Result

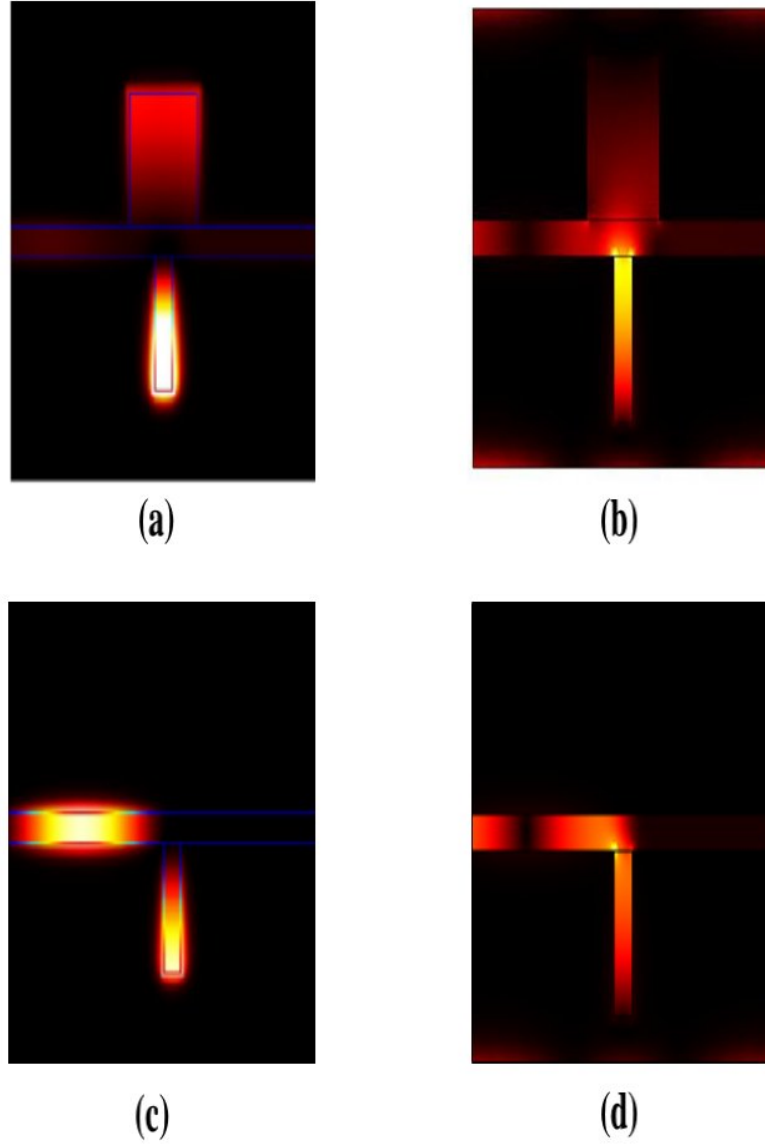


**Figure 4.5:**  $|H_z|^2$  with and without the groove at the resonance wavelength  $\lambda = 1392$  nm (a),(c) by Chen et al. [12] and (b),(d) re-simulated work.

Then the overall variation of refractive index was analyzed to compare the published sensitivity with the calculated result in Fig 4.6 [a-b]. After using sensitivity equation, the calculated result was found to be 1280 nm/RIU. While the published result is 1260 nm/RIU, usually a 2.8 % error is allowed in case of simulation results. So we can say that our simulation setup is less prone in case of sensor simulation.

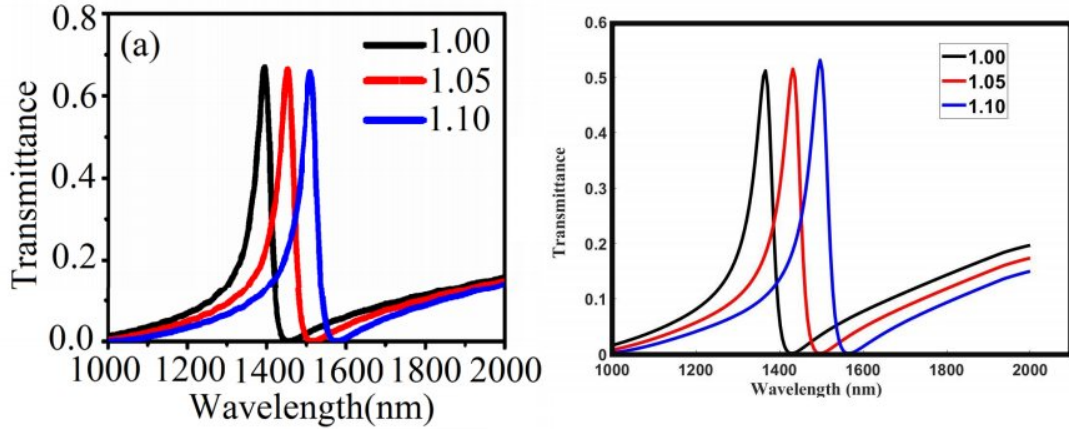


**Figure 4.6:** (a) Chen et al's [12] Transmission profile b) Re-simulated profile

As the error is negligible, our simulation setup can simulate the proposed structures and give proper results .

#### 4.1.2 Resimulation of Demultiplexer

The simulation setup must be validated before designing our own models. So the resimulation of some published papers are verified in this section. **“A T-shaped high resolution plasmonic demultiplexer based on perturbations of two nanoresonators”** proposed by Liu et al. [2], published in *Optics Communications* is resimulated in this section. Figure 4.7 exhibits the structure of the demux and Table-4.2 contains the parameters of the structure.

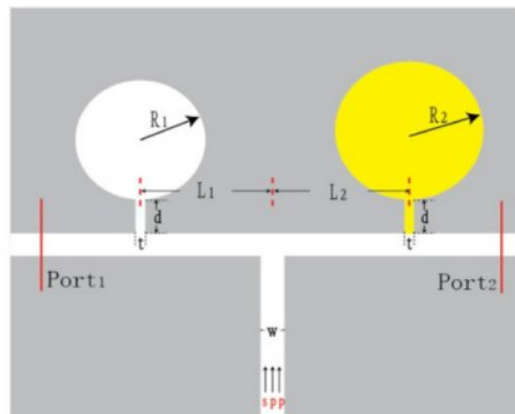


**Figure 4.7:** Demux proposed by Liu et al. [2]

Parameters	Denoted Symbols	Value	Unit
Radius of left resonator	R1	200	nm
Radius of right resonator	R2	210	nm
Center to 1 <sup>st</sup> resonator	L1	490	nm
Center to 2 <sup>nd</sup> resonator	L2	490	nm
Width of narrow insulator slit	t	20	nm
Distance between resonator and waveguide	d	100	nm
Width of waveguide	w	50	nm

**Table 4.2:** Parameters for Liu et al. [2]

The simulation was carried out according to the previously mentioned steps in Fig 4.2. Structure geometry and meshing were observed to be as Fig 4.8 [a-b] respectively. The radius of the two resonator cavities are different which results in the variation of transmission peaks. There is a trade off between high resolution and high transmission efficiency [2]. The performance metric used to measure the quality of the demux is the Quality factor.

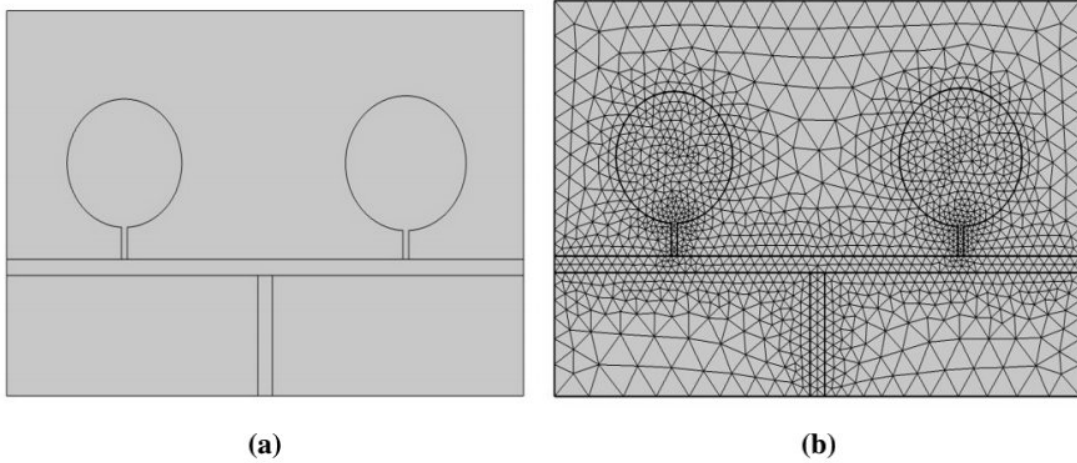


**Figure 4.8:** a) Resimulated geometric structure b) mesh view

Since the structure has 2 ports, the simulation was done two times (one for each port). The transmission spectrum for each port was observed. Figure 4.9 shows the obtained transmission spectrum for the two ports (Port 1 and Port 2).

The two peaks for the two ports are found at 788 nm and 820 nm respectively [2]. Our resimulation provides a peak at 789.6 nm for the right port (port 1) at 75.5 %

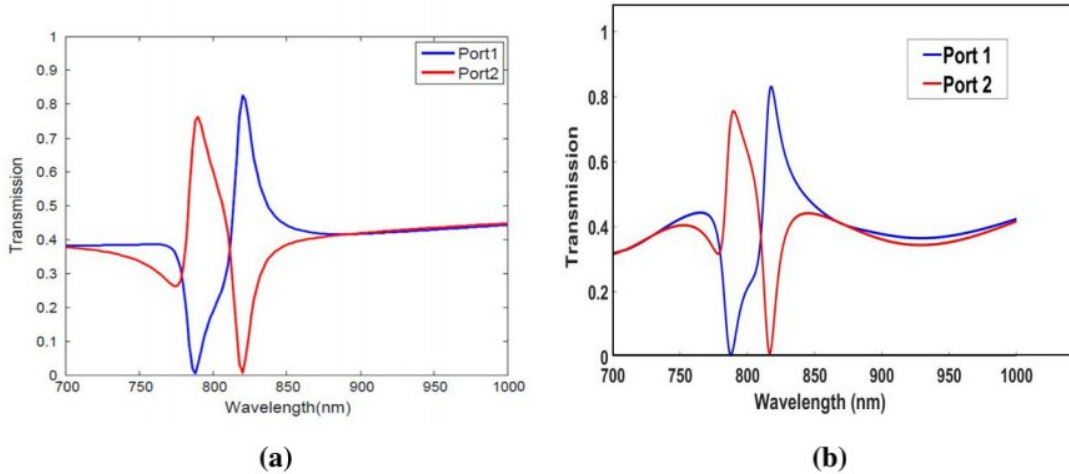


**Figure 4.9:** a) Liu et al.'s [2] result (b) resimulated result

transmission efficiency. Similarly for the left port (port 2), peak is at 817.7 nm with 83 % transmission efficiency. So, our results match with the output of Lie et al. [2]. Thus we can proceed with a similar simulation setup for modeling demultiplexers.

## 4.2 Performance Metrics

To better understand the quality of the sensors, three performance metrics such as Sensitivity (S) , Figure of merit (FOM) and Quality factor (Q-factor) are discussed here. Improving these quantities will result in a better performance and thus improve their applications.

### 4.2.1 Sensitivity (S)

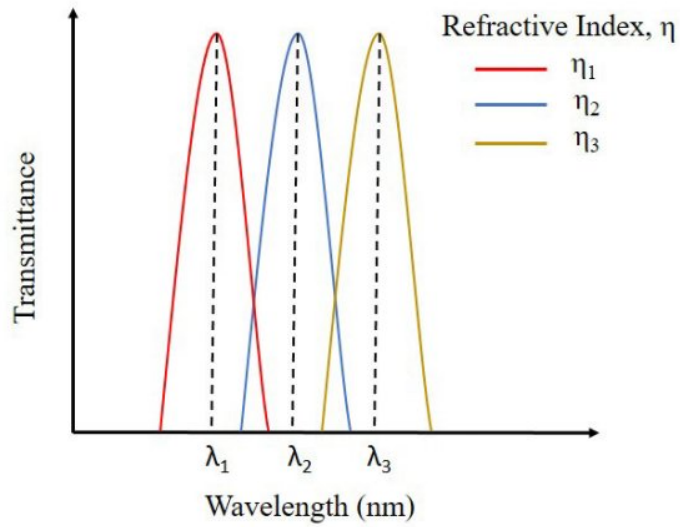


**Figure 4.10:** Sensitivity Calculation

Sensitivity is defined as the ratio of change of resonant wavelength to the change of refractive index [12]. Thus,

$$S = \frac{\Delta\lambda}{\Delta n} \quad (4.1)$$

Where,

$\Delta\lambda$  is the change in wavelength.

$\Delta n$  is the change in refractive index.

Performance of refractive index (RI) sensors are primarily measured by sensitivity. By changing the refractive index, the resonant wavelength can either increase or decrease (denoted by redshift or blueshift). In Figure 4.10 the yellow curve is redshifted from the center blue curve whereas the red curve is blueshifted.

## 4.2.2 Figure of merit (FOM)

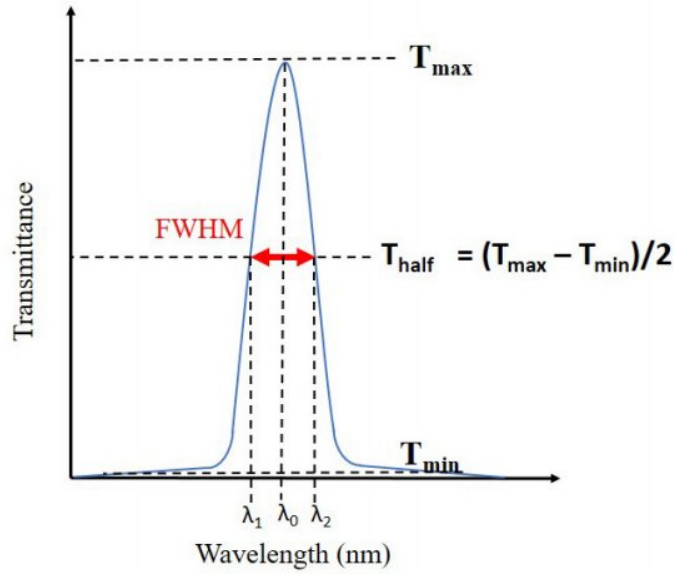


**Figure 4.11:** Figure of merit (FOM) calculation

Another performance metric used to measure the quality of the RI sensors is the Figure of merit (FOM). FOM is defined as follows [12],

$$FOM = \frac{S}{FWHM} \quad (4.2)$$

Where,

S is the sensitivity,

And, FWHM is the Full Width at Half Maximum, which is again defined as the the change of wavelength at half transmission value.

## 4.2.3 Quality Factor (Q-factor)

Mostly for filters and demultiplexers, the performance metric is the Quality factor. It is defined as,

$$Q - factor = \frac{\lambda_{resonant}}{FWHM} \quad (4.3)$$

Where,

$\lambda_{resonant}$  is the resonant wavelength, and

FWHM is the Full Width at Half Maximum.

Fig 4.11 depicts the resonant wavelength as well as the FWHM for a certain wave-shape. Quality factor measures how sharp the peak is. Sharper peaks have greater



Q-factor values. Filtering performances are largely enhanced by high Q-factor peaks. Fig 4.12 shows the difference between High and Low Q-factors

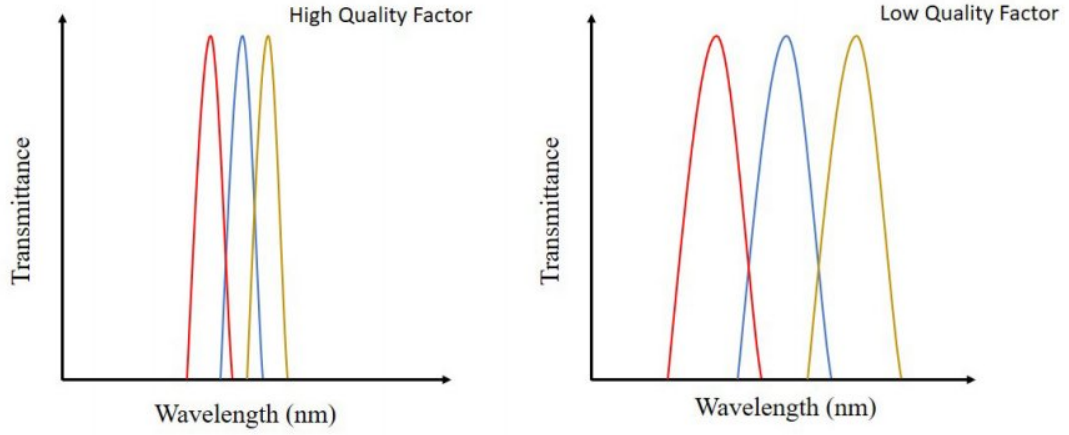


**Figure 4.12:** High Q-factor vs Low Q-factor

### 4.3 Ring and Cavity Resonator

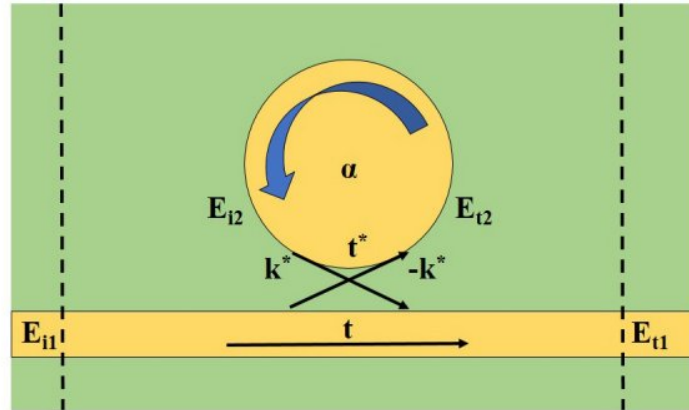


**Figure 4.13:** Schematic of a plasmonic waveguide coupled with a ring structure.

A circular ring structure based simple MIM waveguide with a radius  $R$  is shown in fig. 4.13. Considering lossless, single polarized coupling between the straight waveguide and ring, the input-output relation can be formulated by the matrix [55],

$$\begin{bmatrix} E_{t1} \\ E_{t2} \end{bmatrix} = \begin{bmatrix} t & k \\ -k^* & t^* \end{bmatrix} \begin{bmatrix} E_{i1} \\ E_{i2} \end{bmatrix} \quad (4.4)$$

Where,

$k$  and  $t$  are coupling parameters.

$E_{t1}$  = transmission complex mode amplitude at the output port.

$E_{t2}$  = coupled complex mode amplitude to the cavity.

$E_{i1}$  = source complex mode amplitude at the input port.

$E_{i2}$  = complex mode amplitude transmitted from the cavity.

Various losses occur during the wave propagation in the ring, which are considered in the attenuation constant. The symmetric matrix along the reciprocal essence of the network gives,

$$|k|^2 + |t|^2 = 1 \quad (4.5)$$

$E$  is considered as unity for the simplicity of calculation,

$$E_{i2} = \alpha.e^{j\theta} E_{t2} \quad (4.6)$$

where,  $\alpha$  is the loss coefficient of the ring and  $\theta$  can be states as,

$$\theta = \frac{\omega L}{c} = \frac{2\pi c_0 L}{\lambda_c} = k.n_{eff}.L = \beta.L, \quad (4.7)$$

where  $c = c_0/n_{eff}$  is the phase velocity of the ring,  $n_{eff}$  is the effective refractive index,  $L = 2\pi r$  is the circumference of the ring,  $r$  is the radius of the ring and  $k = 2\pi/\lambda$  is the propagation constant.

From eq[4.4] and eq[4.6], the terms can we written as,

$$E_{t2} = -k^* + t^*(\alpha e^{j\theta} E_{t2}),$$

$$E_{t2}(1 - t^* \alpha e^{j\theta}) = -k^*,$$

$$E_{t2} = \frac{-k^*}{1 - t^* \alpha e^{j\theta}} \quad (4.8)$$

$$E_{t1} = \frac{-\alpha + t e^{-j\theta}}{-\alpha t^* + e^{-j\theta}} \quad (4.9)$$

$$E_{i2} = \frac{-\alpha k^*}{-\alpha t^* + e^{-j\theta}} \quad (4.10)$$

The modal power can be obtained as the square of the complex mode amplitude  $E$ . Transmitted power  $P_{t1}$  at the output waveguide and the circulating power in the ring  $P_{i2}$  can be exhibited on resonance in the following form, having  $\theta + \varphi_t = 2\pi m.$ , where  $t = |t|e^{j\varphi_t}$  is the coupling loss,  $\varphi_t$  denotes the coupling phase, and  $m$  is an integer,

$$P_{t1} = |E_{t1}|^2 = \frac{\alpha^2 + |t|^2 - 2\alpha|t| \cos(\theta + \varphi_t)}{1 + \alpha^2|t|^2 - 2\alpha|t| \cos(\theta + \varphi_t)} = \frac{(\alpha - |t|)^2}{(1 - \alpha|t|)^2}, \quad (4.11)$$

$$P_{i2} = |E_{i2}|^2 = \frac{\alpha^2(1 - |t|)^2}{(1 - \alpha|t|)^2} \quad (4.12)$$

From eq[4.7], the resonant wavelength  $\lambda_m$  can be found as,

$$\frac{2\pi}{\lambda_m} \cdot n_{eff} \cdot L = 2\pi \left( m - \frac{\varphi_t}{2\pi} \right) \quad (4.13)$$

$$\lambda_m = \frac{n_{eff} \cdot L}{m - \left( \frac{\varphi_t}{2\pi} \right)} \quad (4.14)$$

# Chapter 5

## Design, Optimization and Performance Analysis of the Proposed Devices

### 5.1 Sensor Design with U shaped cavity coupled with a subannular circle

#### 5.1.1 Structure Layout

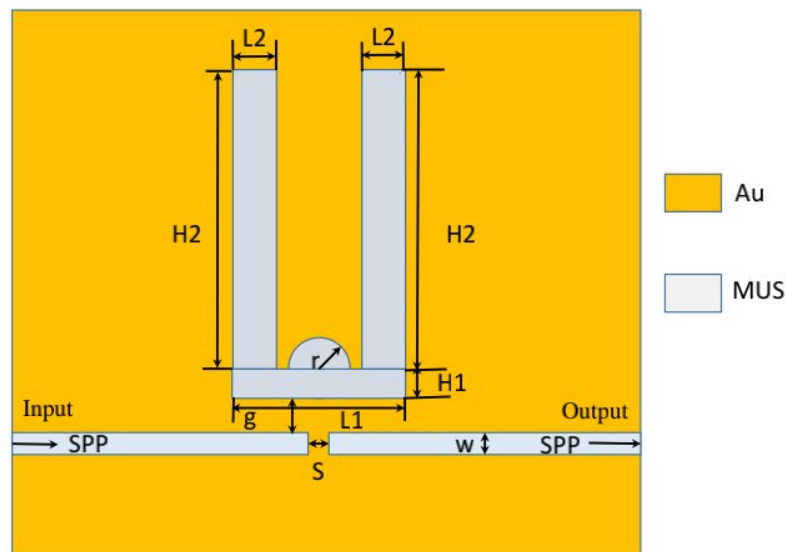


Figure 5.1: 2D model of the proposed structure

The 2D configuration of the proposed sensor is given in Figure 5.1. The nanosensor setup consists of a MIM waveguide with a baffle in the middle and a vertically coupled U shaped cavity consisting of a subannular circle in the center of the U shaped cavity. Table 5.1 lists the preliminary parameters used in the 2D modeling of the proposed schematic. The white color in Figure 5.1 represents the material under sensing (MUS), which is filled within the cavities and cores of the waveguide. Similarly, the golden

yellow color in the schematic denotes the use of gold as the metallic base.

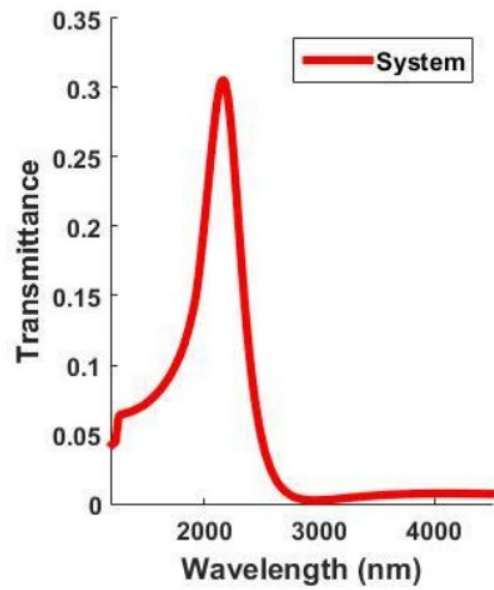
Parameters	Symbol	Value (nm)
Width of waveguide	w	20
Length of vertical bars	$L_2$	50
Length of horizontal bar	$L_1$	200
Length of vertical bars	$H_2$	350
Height of horizontal bar	$H_1$	30
Radius of semi-circular cavity	$r_1$	25
Gap of resonator from waveguide	g	10
Length of baffle	S	10

**Table 5.1:** Structural parameters

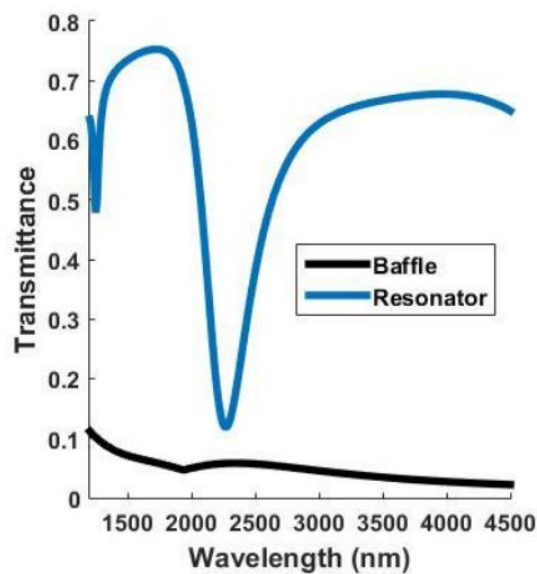
As COMSOL Multiphysics is utilized for simulating the proposed structure, Finite Element Method (FEM) model of solution is followed here. During simulation, two monitors named  $P_{input}$  and  $P_{output}$  are placed at the input and output port respectively, to observe the SPP flows. By observing the results from the monitors, Transmittance can be easily calculated as  $T = \frac{P_{input}}{P_{output}}$

### 5.1.2 Initial Transmission spectrum and results

Taking the MUS to be a material with refractive index of 1.0, the structure is simulated with the help of COMSOL Multiphysics software. Figure 5.2a depicts the transmittance spectrum of the initial simulation. The resonant peak occurs at 2158.3 nm. Furthermore, the sharp, asymmetrical profile of the peaks indicates the presence of Fano resonance.



(a)



(b)

**Figure 5.2:** a) Transmission spectrum of the system b) Effect of the Baffle and Resonator on system spectrum

A Fano resonance is quite different from a typical Lorentzian curve. It is so because, in case of a Fano resonance, the transmission profile is asymmetrical unlike the symmetry of the profile in case of a Lorentzian curve. This sort of resonance is produced mainly from the interference between the narrow band and the wide band.

In case of the proposed structure, it can be observed from fig. 5.2 (b) that the narrow band is produced due to the effect of the U shaped resonator cavity coupled with the waveguide and the wide band is produced when there is only a baffle. So, due to the interference between the narrow band and the wide band produced by the resonator cavity and the baffle, the asymmetric transmission profile is generated.

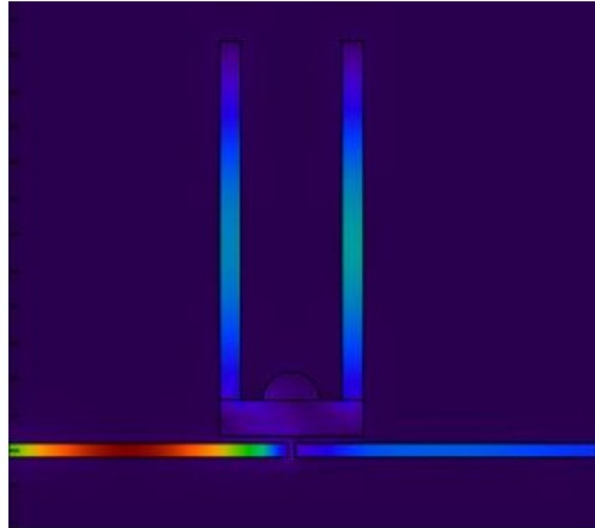


**Figure 5.3:**  $|H_z|^2$  field distribution for the presented MIM sensor

It can be seen from Fig 5.2(a), that the transmittance is in the range of 0.3 to 0.4, this is very low. It can be understood if the field plot of the proposed structure is analyzed. Fig.5.3 represents the field distribution. As it can be seen that most of the energy is trapped within the waveguide before the baffle part. While in the output port, comparatively less energy flows through. Due to this, there is a reduced transmittance for the transmitted signal. But, as it has been stated before, researchers focus mainly on optimizing the sensitivity compared to other performance indices, so it should not be a matter of issue. Also, transmittance can be easily amplified as there are ample devices to achieve that.

Now the sensitivity of the proposed sensor has to be calculated for the initial parameters according to Table 5.1. In order to calculate the sensitivity, firstly, the refractive index has to be varied over the wavelength. In Fig 5.4, it can be observed that 5 curves have been obtained for refractive index values of 1.0 to 1.1 with a step of 0.25.

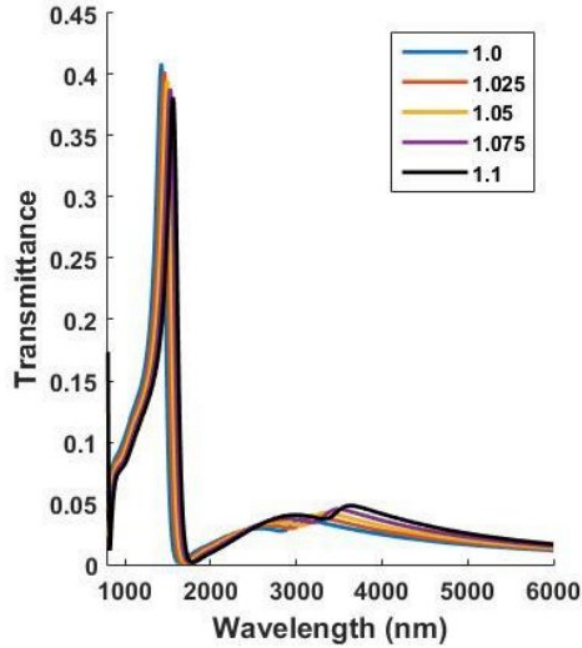


**Figure 5.4:** Initial refractive index variation

Now the sensitivity can be calculated according to eqn 4.1, mentioned in Section 4.2.1 of Chapter 4. After calculating, the sensitivity was found to be 1320 nm/RIU which is quite low. In the next section, the structural parameters are optimized to obtain a sensor with better sensitivity compared to the acquired results of this section.

### 5.1.3 Optimization for gaining Maximum sensitivity

In order to obtain optimal performance, the parameters mentioned in Table 5.1 have to be optimized. After extensive simulations, it was found that only 4 of the 8 features, mentioned above, greatly influences the performance of the structure. These are Length of the vertical slab (L2), Height of the vertical slab (H2), Height of the horizontal slab (H1), and the radius of the subannular circular cavity (r1). The parameters were optimized after observing the change of the peak resonant wavelength for the respective parameters.

First of all, the length of the vertical slab is optimized. In order to do that, a parametric sweep analysis was done by keeping the other parameters unchanged. Here the value of L2 was swept from 30 nm to 50 nm with a step size of 5 nm. The transmission spectrum is obtained according to fig 5.5(a). After that the respective peaks were analyzed to find out at which resonant wavelengths, the peak occurs.



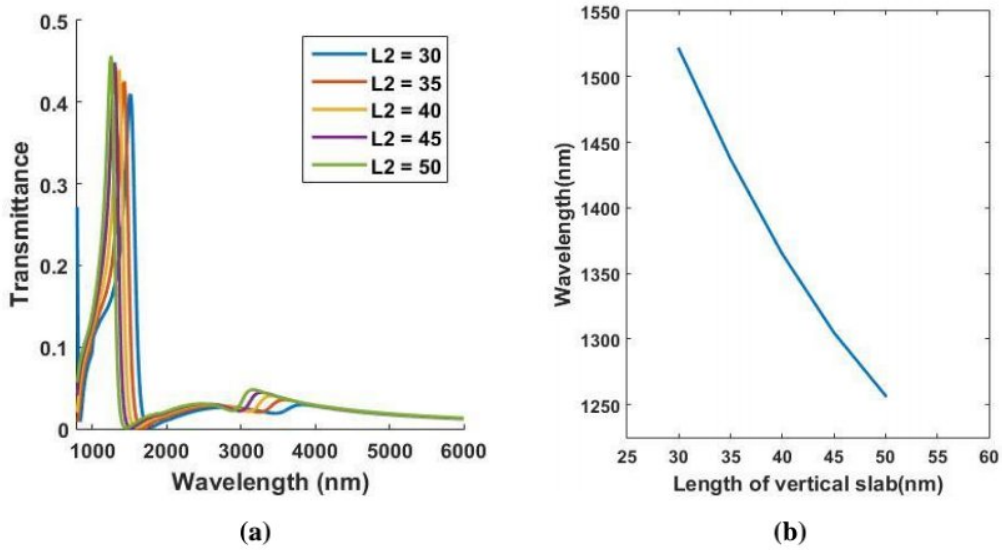


**Figure 5.5:** a) Transmission spectrum for different values of L2 b) Relation between L2 and the resonant wavelengths

Fig 5.5 (b) represents the relationship between the resonant wavelength shift due to the variation of the length of the vertical slab. It can be observed that there is a large blueshift due to the variation, meaning the smaller the Length, the better the result as Sensitivity tends to be larger at higher resonant wavelengths. The resonant wavelength decreases by a step of 85 nm approximately. So for this step, the optimized value for L2 will be 30 nm

Next, the height of the vertical slab is varied from 350 nm to 500 nm, with a step of 37.5 nm. Unlike the previous step, here the value of L2 will be the optimized value i.e., 30 nm instead of 50 nm. The other parameters will be unchanged. If the transmission spectrum from fig 5.6(a) is observed, it can be noticed that the shift is higher for the variation of the height of slab compared to its length. Unlike the previous case, here a large redshift is observed if the height is varied. Due to redshift, improved results can be obtained for the higher values. From fig 5.6(b), it can be seen that, 500 nm give the largest shift. So, the optimized height selected for this structure is 500 nm.

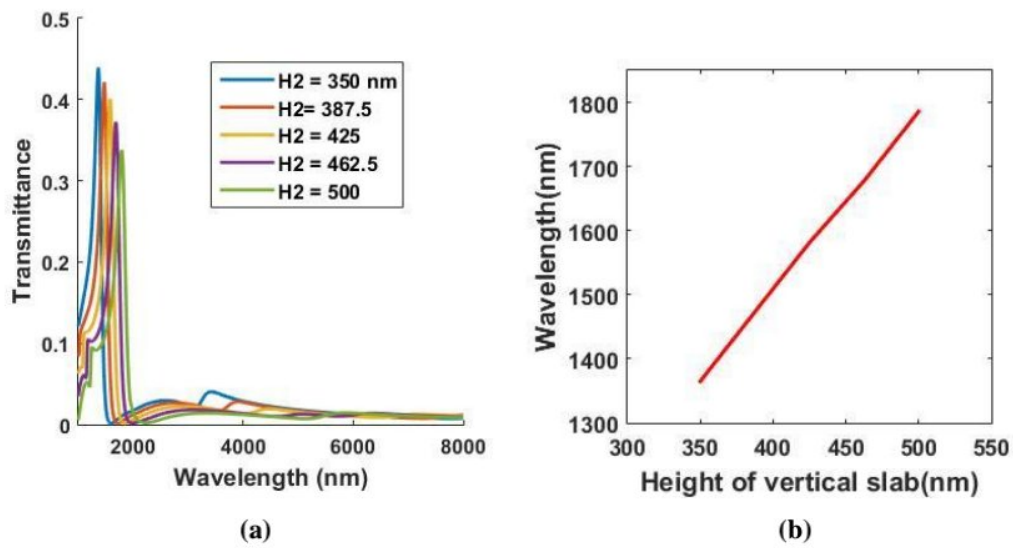


**Figure 5.6:** a)Transmission spectrum for different values of  $H_2$  b) Relation between  $H_2$  and the resonant wavelengths

Similarly, like the previous case, the radius of the sub annular circular cavity, that is directly coupled to the horizontal slab, is to be varied. The radius has been varied from 30 to 45 nm with a step of 5 nm. In this case, as observed from fig. 5.7(a), the transmission spectrum shift is very small. It can be observed further clearly, if the relation between the resonant wavelength and the radius is observed. It can be seen that the redshift is quite small. The shift was found to be around 12 nm. After the analysis is completed, the optimized parameter was selected to be 45 nm.

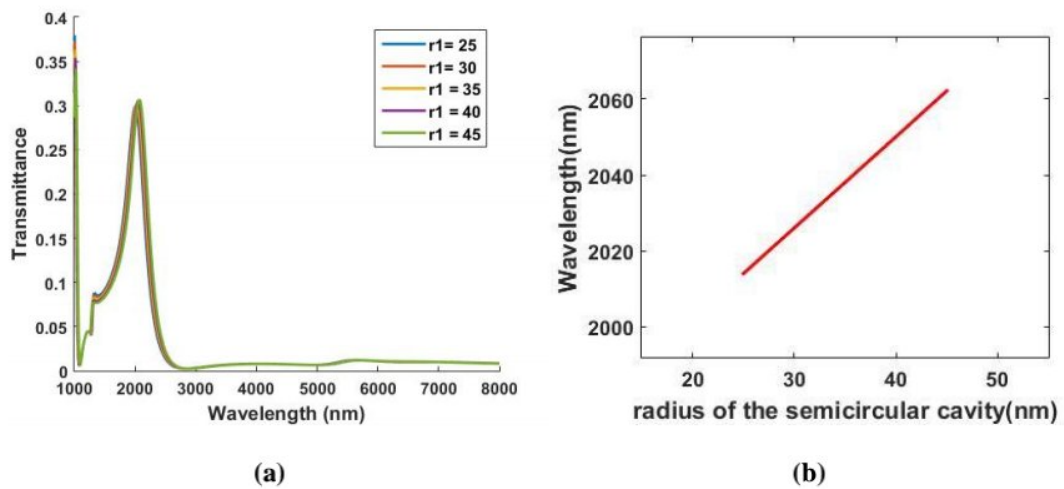


**Figure 5.7:** a)Transmission spectrum for different values of  $r_1$  b) Relation between  $r_1$  and the resonant wavelengths

Lastly, like the previous steps, the height of the horizontal rectangular slab was varied with a step of 5 nm from 30 nm to 50 nm. Here, the relationship curve found in fig.5.8(b) is a redshift which is larger compared to the variation of the radius of the semi circular cavity. The resonant wavelength shift was found to be around 25 nm approximately.

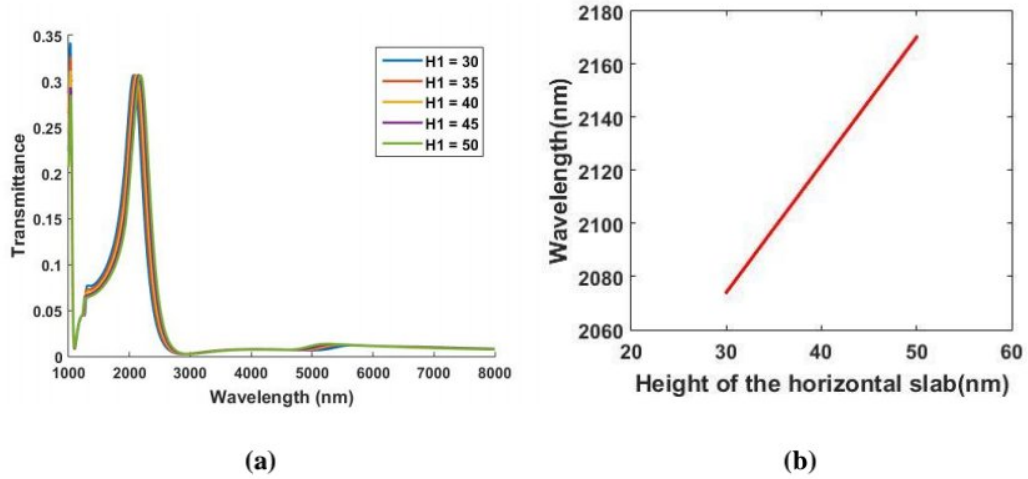


**Figure 5.8:** a) Transmission spectrum for different values of  $H_1$  b) Relation between  $H_1$  and the resonant wavelengths

After analyzing the simulation results, it can be observed that out of the 4 optimized parameters, height of the horizontal slab shows the most phase shift compared to the other parameters analyzed.

Now the final optimized parameters are depicted in the following table Table 5.2

Parameters	Initial Values	Optimized Values
$L_2$	50	30
$H_2$	350	500
$r_1$	25	45
$H_1$	30	50

**Table 5.2:** Final optimized parameters

After simulating the optimized structure, the transmission spectrum was simulated as Fig 5.9

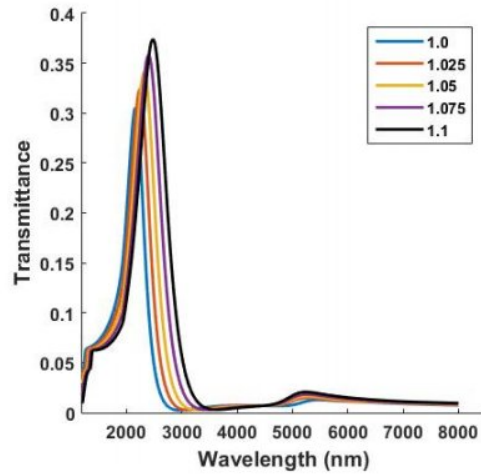


**Figure 5.9:** Finalized Transmission Spectrum

Again calculating sensitivity, the result was found to be around 3120 nm/RIU which is vastly improved compared to previous result. Also, as the metal base being used is gold, the objective previously stated has been fulfilled. In the next section, the proposed sensor is being applied in various fields in order to measure its practical viability.

#### 5.1.4 Temperature sensor

As stated previously, optical sensing is basically quantizing the state of the environment in terms of change of refractive index. So, a typical optical sensor can be used for temperature sensing purpose. Zhu et al. in his proposed paper theorocrafted the relation between temperature and refractive index by selecting the MUS to be PDMS (Polydimethylsiloxane) [56].

$$n_{PDMS}(T) = 1.4167 - 4.5 \times 10^{-4} \cdot T \quad (5.1)$$

If the necessary temperature is given as input, then the corresponding refractive index is easily acquired. For the proposed simulation, temperature is varied from 20° C to 60° C with a step size of 10°

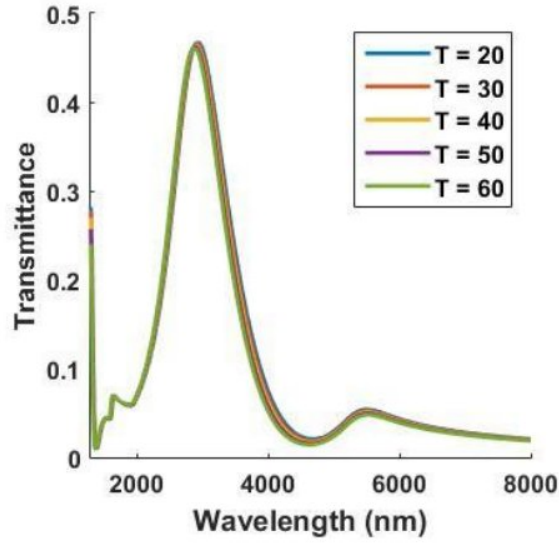


**Figure 5.10:** Transmission spectrum for different temperatures

After analyzing the transmission spectrum, the sensitivity was found to be around  $-1.2nm/^{\circ}C$  which is quite good. So the proposed structure is a good temperature sensor.

## 5.2 Filter design with triple ring resonators, each having triple stubs

### 5.2.1 Structure layout

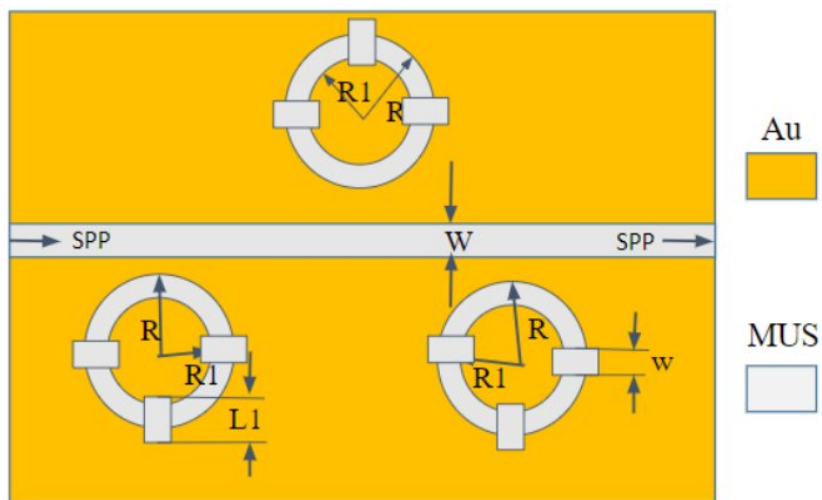


**Figure 5.11:** 2D model of the proposed filter

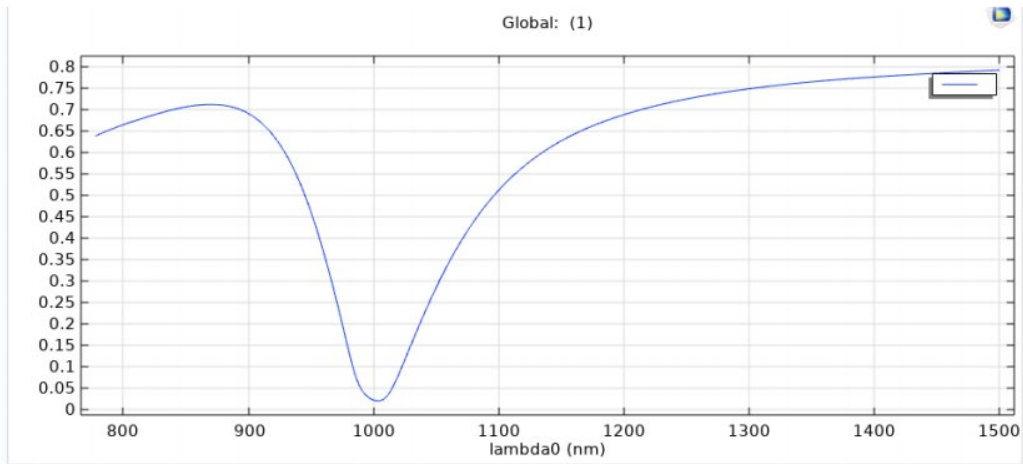
A 2D confrontation of our 3rd proposed structure is given in figure 5.11. It is a nanoplasmonic MIM filter consisting of 3 circular ring resonators of equal dimensions. Each circular ring resonator consists of 3 rectangular stubs of similar dimensions. The radii of the inner circles is denoted by R1, whereas the radii of the outer circles is denoted by R2. The width and length of the rectangular stubs are denoted by w1 and L1 respectively. The off white color in fig. 5.11 represents air, which is filled within the cavities of the resonators and cores of the waveguide. The goldish yellow color in the schematic denotes the use of gold as the metallic base. Table 5.3 lists the preliminary parameters used in the 2D modeling of the proposed schematic.

Parameters	Symbol	Dimension
Width of the waveguide	W	50
Outer radius of all circles	R	75
Inner radius of all circles	R1	45
Width of stubs	w	15
Length of stubs	L1	40
Gap of resonator from waveguide	g	15
Distance of 2 circular centers	d	432.5

**Table 5.3:** Structural Parameters for the proposed filter

COMSOL Multiphysics 5.6 is a commercially available multiphysics simulation and finite element analysis (FEM) software that runs on any platform. It supports both traditional physics-based user interfaces and connected partial differential equations systems.

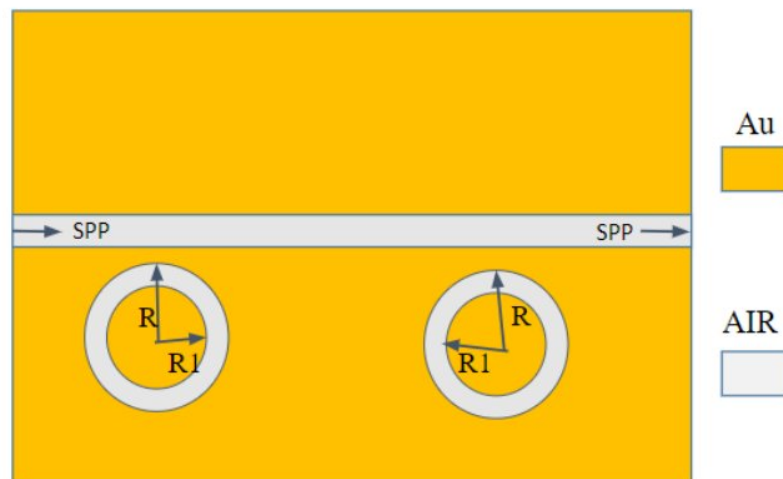
During simulation, two monitors named  $P_{input}$  and  $P_{output}$  are placed at the input and output port respectively, to observe the SPP flows. By observing the results from the monitors, Transmittance can be easily calculated as  $T = \frac{P_{input}}{P_{output}}$



**Figure 5.12:** 2D model of the proposed filter

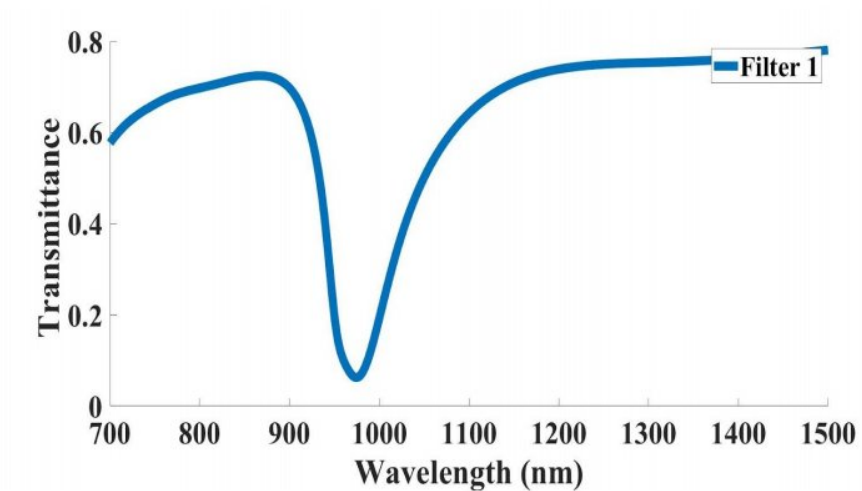
### 5.2.2 Result analysis of double ring resonators

When the basic magnetic mode excites the surface plasmon, it propagates via the straight waveguide on the MIM structure. The circular ring cavities' resonant condition is satisfied by the incident wavelength. The circular ring cavities will couple the energy of the straight waveguide cavity to produce filtering performance. At first the geometric structure of a basic filter of this design is shown in Fig. 5.13. The two circular ring resonators have the same inner and outer radii and are filled with air (RI=1.5).



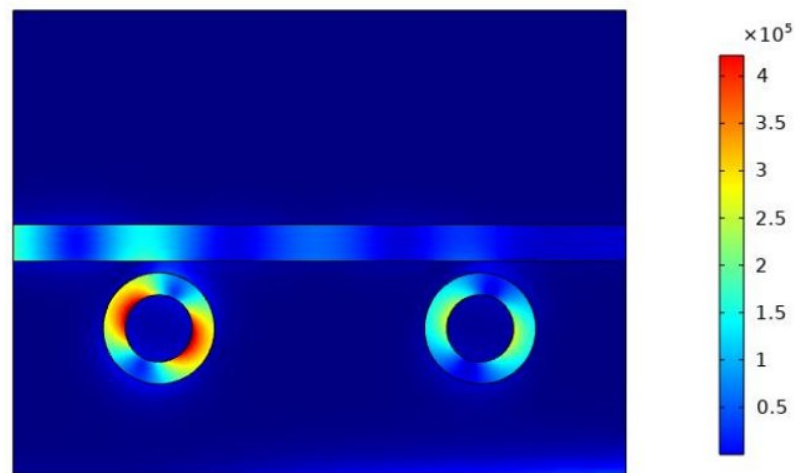
**Figure 5.13:** Double ring resonator filter (Filter 1)

Fig 5.14 shows that the SPPs wave transmission characteristic curve is detected at the outlet of the waveguide over the circular ring cavities. This curve's wavelength range corresponds to 700 nm –1500 nm.



**Figure 5.14:** Initial transmittance curve for filter 1

A transmission dip of 0.062 is observed at the wavelength of 974.7 nm. There is essentially little magnetic field at the exit because the energy is concentrated in the ring cavity, forming an obvious standing wave that is difficult to propagate. The corresponding magnetic field graph is shown in Fig. 5.15



**Figure 5.15:**  $|H_z|^2$  field spectrum for filter 1

The change graph of the filter curve generated by altering the radius (R1) of the inner ring of the resonators ring reveals that when the radius increases, the filter curve shows a blue shift, and the minimum transmission continues to increase. These are shown in Figure 5.16



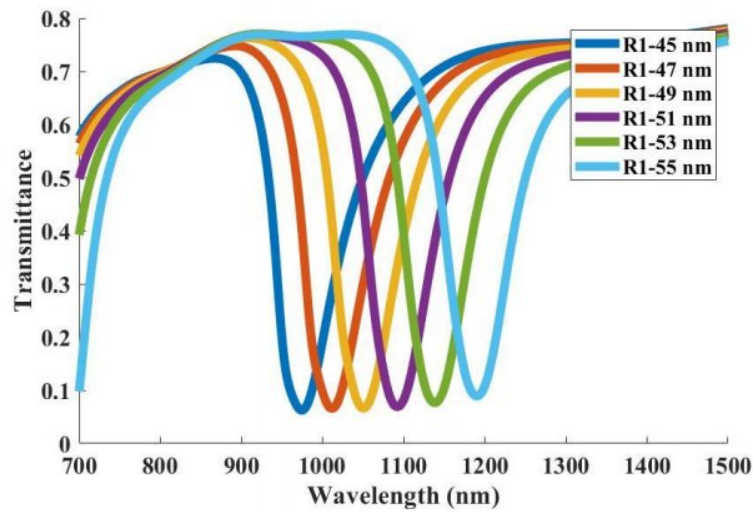


**Figure 5.16:** Transmission spectrum for different values of R1 in filter 1

### 5.2.3 Result analysis of double ring resonators with stubs

To increase the performance of the filter, rectangular stubs are added to the resonators. Here each circular ring has 3 stubs. This filter is referred to as filter 2 and it consists of circular resonators, stubs and a straight waveguide with two openings. Fig. 5.17 shows filter 2.

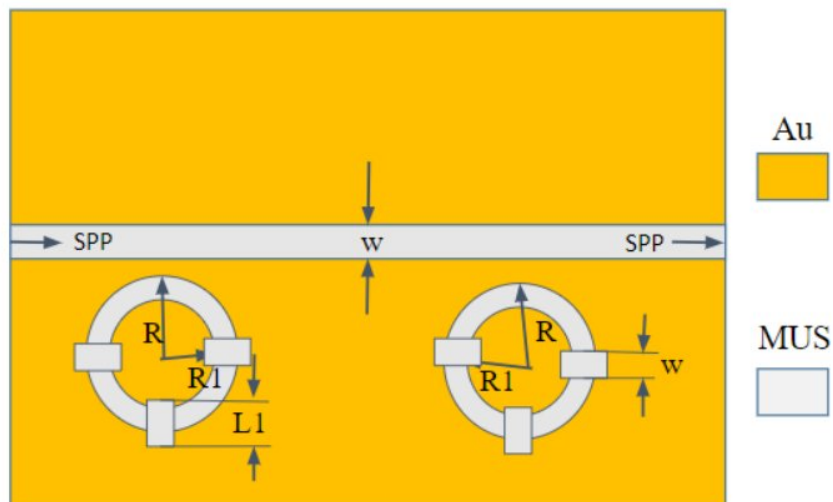


**Figure 5.17:** Double ring resonator filter with stubs (Filter 2)

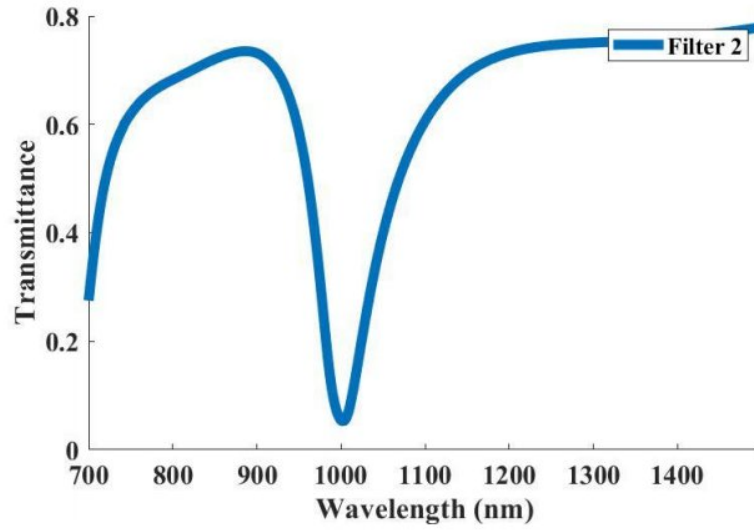


**Figure 5.18:** Initial transmittance curve for filter 2

Figure 5.18 shows the transmittance curve of filter 2. The structure achieves efficient filtering when the incident wavelength is 1003 nm. Here the minimum transmission is 0.052 which is lower than filter 1. Hence the structural design of filter 2 is more efficient.

Fig. 5.19 shows the magnetic field of the filter resonator when the incident wavelength is 1003 nm of the magnetic field distribution. At the extremities of the ring resonator, the energy produces a stable standing wave, which has a stronger filtering effect.

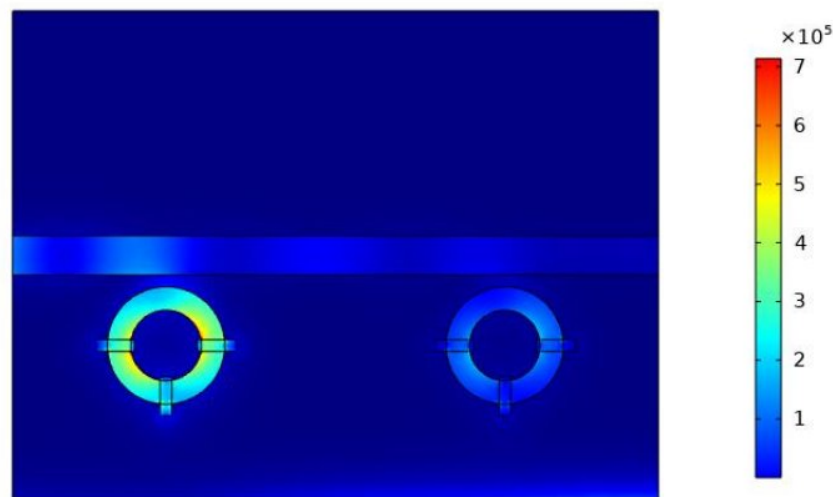


**Figure 5.19:**  $|H_z|^2$  field spectrum for filter2

Now the variation curve of the filtering effect obtained by changing the length of

the rectangular cavity is shown in Fig. 5.20. The lowest transmission will increase as the length of the rectangular stubs increase, and the filtering position will exhibit an equal to the distance redshift.

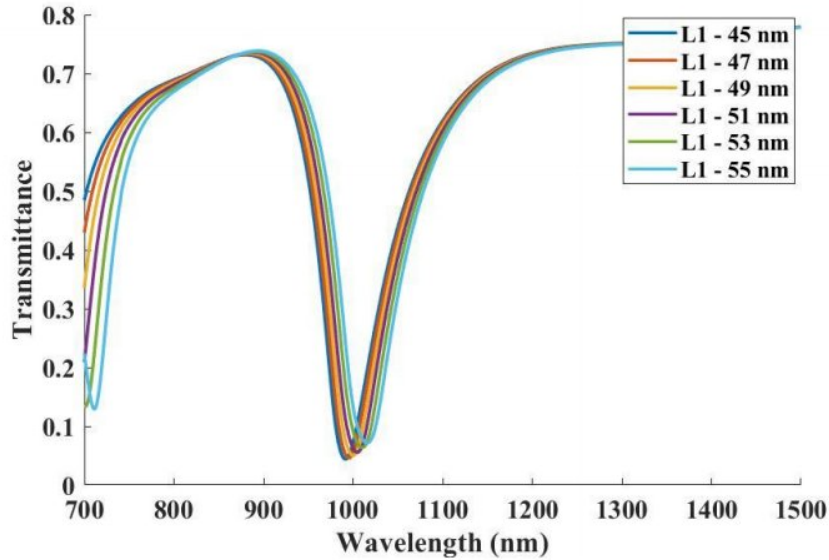


**Figure 5.20:** Transmission values for different values of L1 of filter 2

#### 5.2.4 Result analysis of triple ring resonator filter

Now we will improve the performance of our filter by adding a similar ring resonator on the other side of the waveguide. The filter is referred to as filter 3 and is shown in Fig. 5.21. All 3 resonators are at the same distance away from the straight waveguide. The inner and outer radii of all 3 resonators are equal.

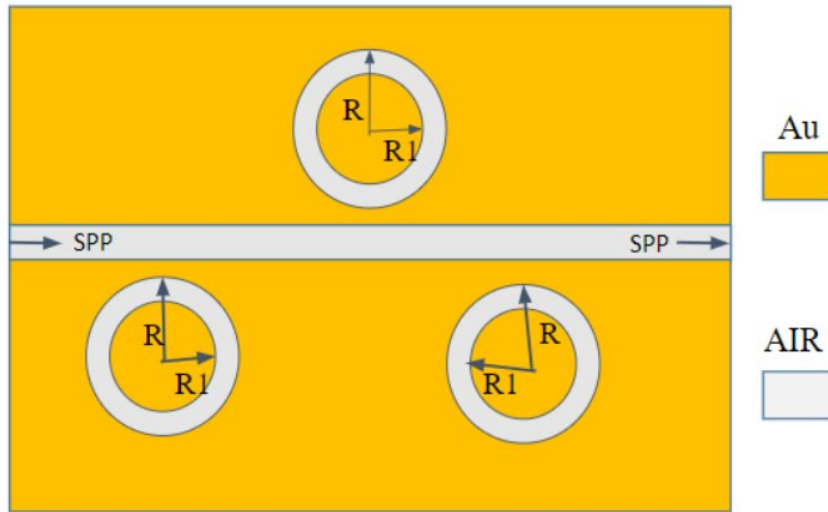


**Figure 5.21:** triple ring resonator filter (Filter 3)

Fig. 5.22 shows the transmission figure obtained by the filter adjusting the structure of the triple circular ring resonators without the rectangular stub resonator cavity in filter 3. The minimum transmission of the structure is very efficient with a value of 0.0027 at the wavelength of 894.5 nm. The shifting curve of the triple ring resonators show that with the increase of radius of the inner circles of the resonators, the lowest transmission value will increase and the filtering position represents redshifts.

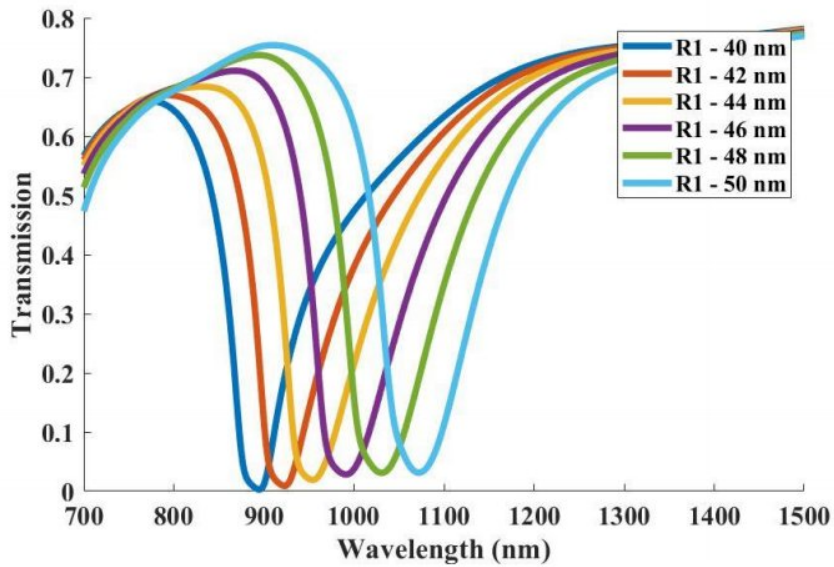


**Figure 5.22:** Transmission values for different values of R1 in filter 3

After obtaining promising results with 3 resonators, we will now further increase the performance of the filter by using rectangular stubs.

### 5.2.5 Result analysis of triple ring resonator filter with stubs

Using the inner radius of filter 3 as  $R_1=40$  nm, we will now implement our final design. Figure 5.23 shows filter 4 of this work as the final design of the filter to be implemented, having 3 rectangular stubs per circular ring resonator.

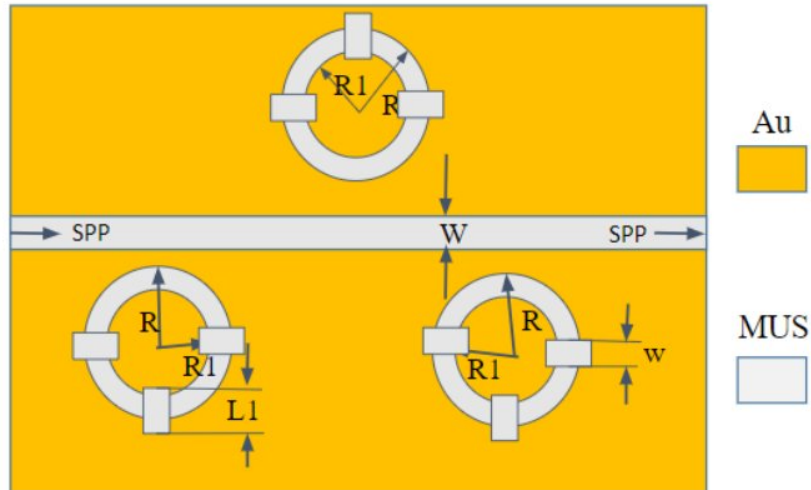


**Figure 5.23:** Triple ring resonator filter with stubs (Filter 4)

The minimum transmission obtained is 0.0023 at the wavelength of 912.5 nm. The magnetic field of the filter 4 resonator when the incident wavelength is 912.5 nm is shown in Fig. 5.24. Here we can clearly observe that most of the SPPs are concentrated in the filter resonator closest to the input port. Gradually the other 2 resonators also block the energy. At the end, in the outer region, we can observe that very negligible amount of energy is passing out. Figure 5.25 shows the filter 4 transmission and the dip shows our best possible result.

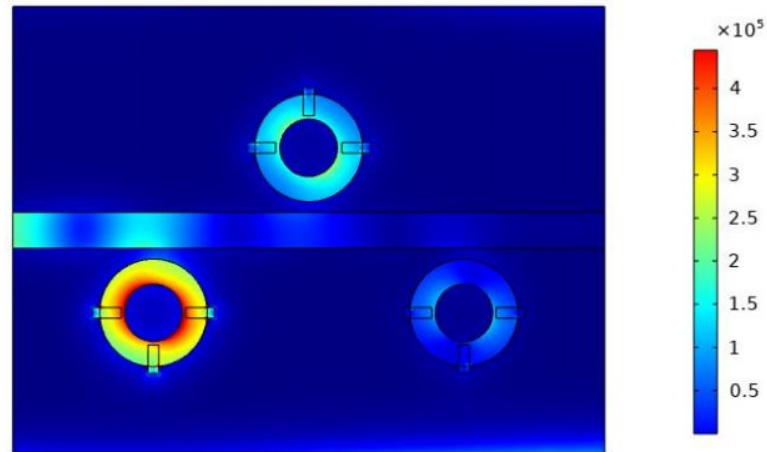


**Figure 5.24:**  $|H_z|^2$  field distribution for filter 4

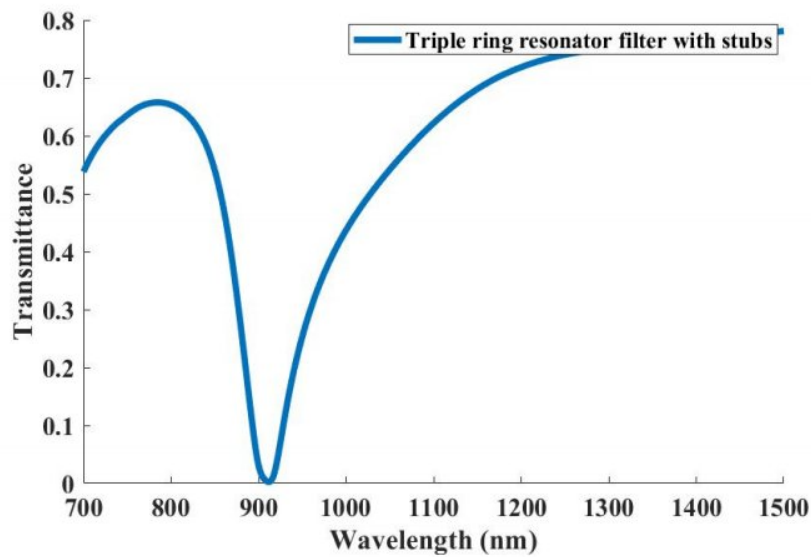


**Figure 5.25:** Initial transmittance curve for filter 4

Now the inner radius of the triple circular ring resonators is kept fixed at  $R1 = 40$  nm and the length of the rectangular stubs is swepted from 40 nm to 50 nm with a step size of 2 nm. We can observe from Fig. 5.26 that as the length of the stubs decreases, the filtering curve corresponds to blueshifts. After testing the performance of the filter with respect to the minimum transmission, it is found that the highest efficiency is obtained when the wavelength of the incident energy is 912.5 nm and the resulting minimum transmittance is 0.0023 nm.

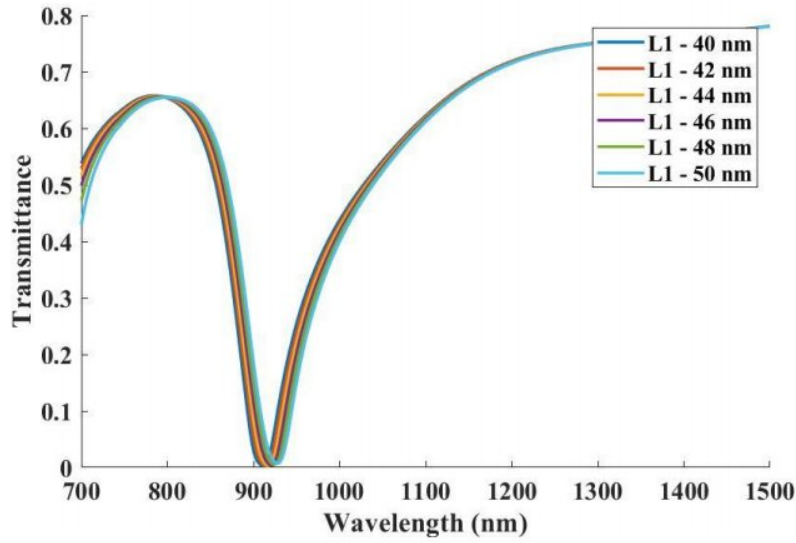


**Figure 5.26:** Transmission values for different values of L1 in filter 4

Finally after proper analyzing of various parameters of the filter, the optimized parameters for highest performance of the filter are found out. They are summarized in table

Parameters	Initial Values	Optimized Values
L1	55	40
R1	55	40

**Table 5.4:** Optimized Parameters for finalized filter

Hence, we can conclude that a highly efficient plasmonic filter was constructed after proper optimization. A final minimum transmittance of 0.0023 was obtained. It can be used in various applications related to filtering such as color filter to filter out energies of desired wavelength.

## 5.3 Concentric ring and nanodisk resonator for wavelength multiplexing

### 5.3.1 Structure Layout

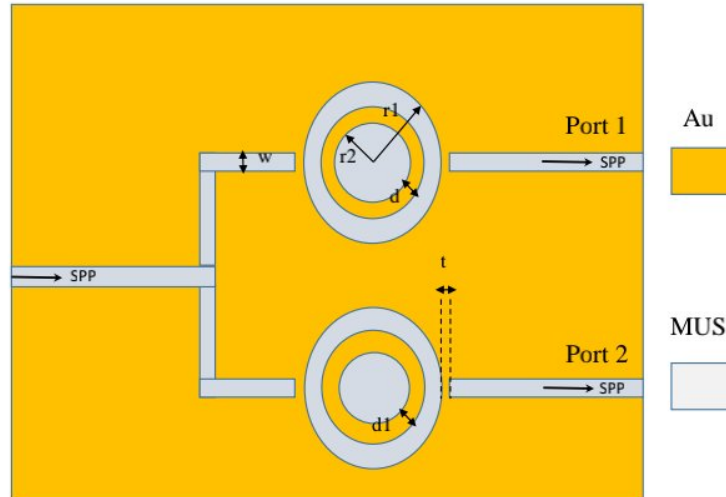


**Figure 5.27:** 2D model of the proposed demultiplexer

Fig 5.27 depicts the configuration of the proposed demultiplexer. The demux consists of MIM waveguides with two resonators for each output port. Each resonator contains a circular ring and a nano-disk in the center. From each of the resonators there is an output waveguide which reaches the output terminal of the structure.

Table 5.5 lists the preliminary parameters used in the 2D modeling of the proposed schematic. The white color in fig. 5.5 represents the material under sensing (MUS), which is filled within the cavities and cores of the waveguide. Similarly, the golden yellow color in the schematic background denotes the use of gold as the metallic base.



Parameter	Symbol	Value (nm)
Width of the waveguide	w	50
Radius of outer disc	$r_1$	260
Radius of inner disc	$r_2$	120
Thickness of the gold ring	d	50
Coupling distance	t	15
Thickness of the gold ring of bottom resonator	$d_1$	60

**Table 5.5:** Structural parameters for demux

The simulation of the structure is done in COMSOL Multiphysics 5.6, which is a commercially available multiphysics simulator and uses finite element analysis (FEM) software that runs on any platform. It supports both traditional physics-based user interfaces and connected partial differential equations systems.

During simulation, two monitors named  $P_{input}$  and  $P_{output}$  are placed at the input and output port respectively, to observe the SPP flows. By observing the results from the monitors, Transmittance can be easily calculated as  $T = \frac{P_{input}}{P_{output}}$

### 5.3.2 Initial Transmission spectrum and results

For each port the transmission spectrum is observed. Figure 5.28 depicts the transmittance spectrum of the initial simulation for two ports combined. The transmission peaks are nearly symmetrical which gives a presence of Lorentzian response.

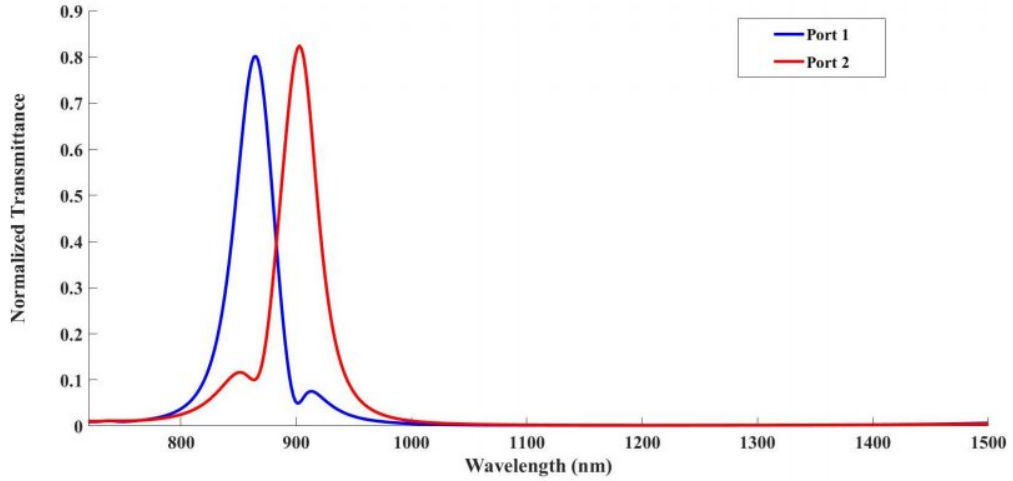


**Figure 5.28:** Transmission spectrum for the two channels

The resonant peaks occurs at 865 nm and 903 nm respectively. The difference between the two peaks gives us the wavelength separation between the two demux channels which is 38 nm. This value is relatively small compared to the other proposed structures in the literature review.

For the better visualization of the channeling of the demux, the magnetic field spectrun is observed.

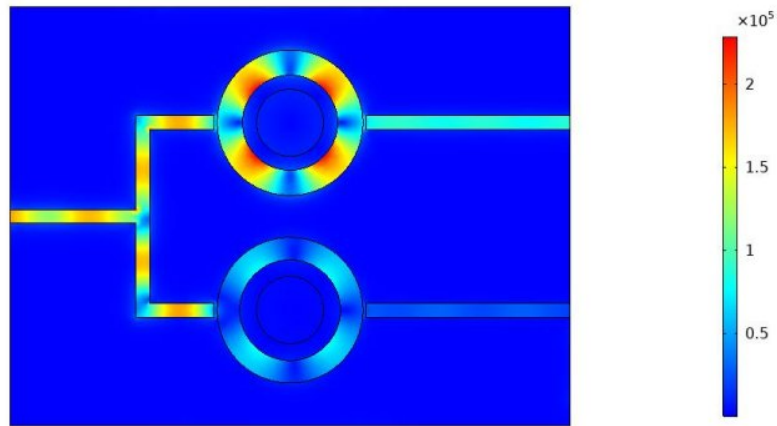


**Figure 5.29:**  $|H_z|^2$  field distribution for port 1 at  $\lambda = 865nm$

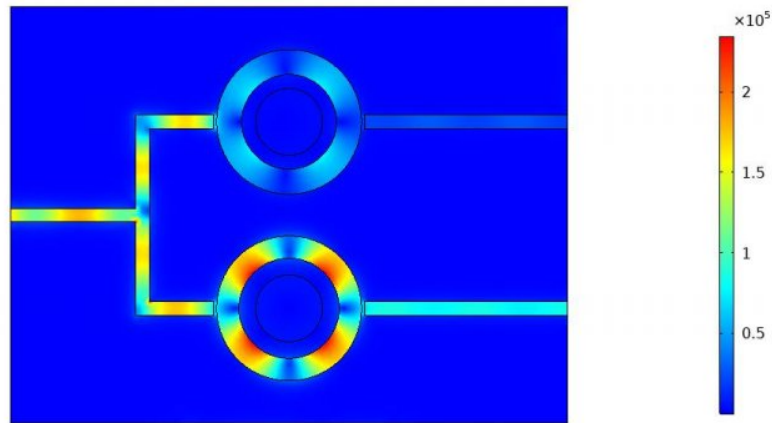


**Figure 5.30:**  $|H_z|^2$  field distribution for port 2  $\lambda = 903nm$

The performance of the demux is measured by a factor called Quality factor (Q-factor) which is defined as,  $Q - factor = \frac{\lambda_{resonant}}{FWHM}$ . The initial transmission graphs give us a low quality factor value of 10 and 12 for port 1 and port 2 respectively.

### 5.3.3 Improving the channeling and Quality factor

Two of the very popular ways of shifting the wavelength of the demux channeling is to change the geometric parameters and also by changing the material used in the resonators.

By changing the refractive index of Port 1 from  $n = 1$  to  $n = 1.1$  with step size of 0.025, a redshift is obtained in the transmission spectrum.

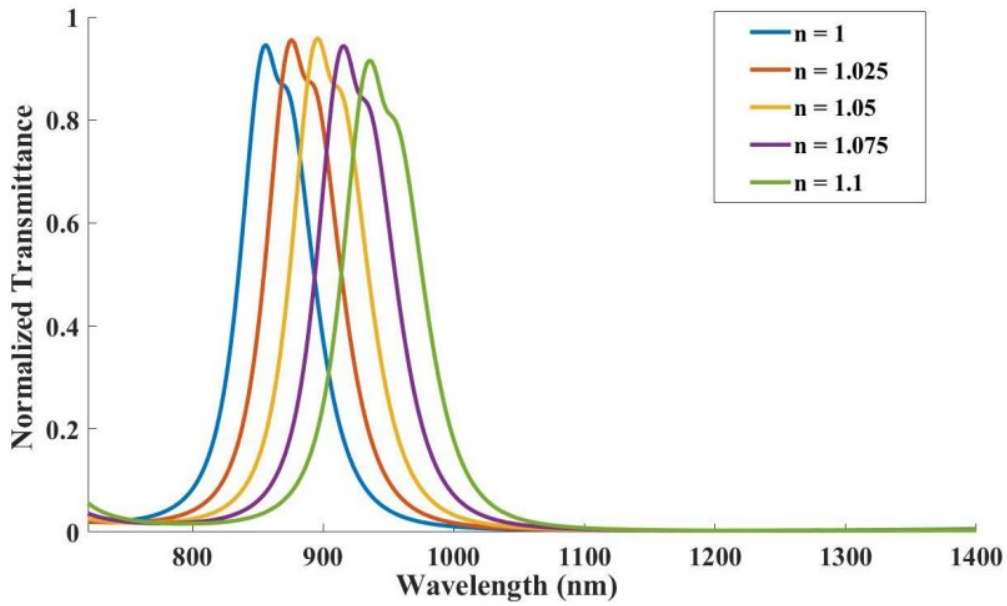


**Figure 5.31:** Varying the RI from 1 to 1.1 for port 1

The width of the inner gold ring is changed from decreased from 70 nm to 50 nm and the shifting of the wavelength is observed in figure 5.32

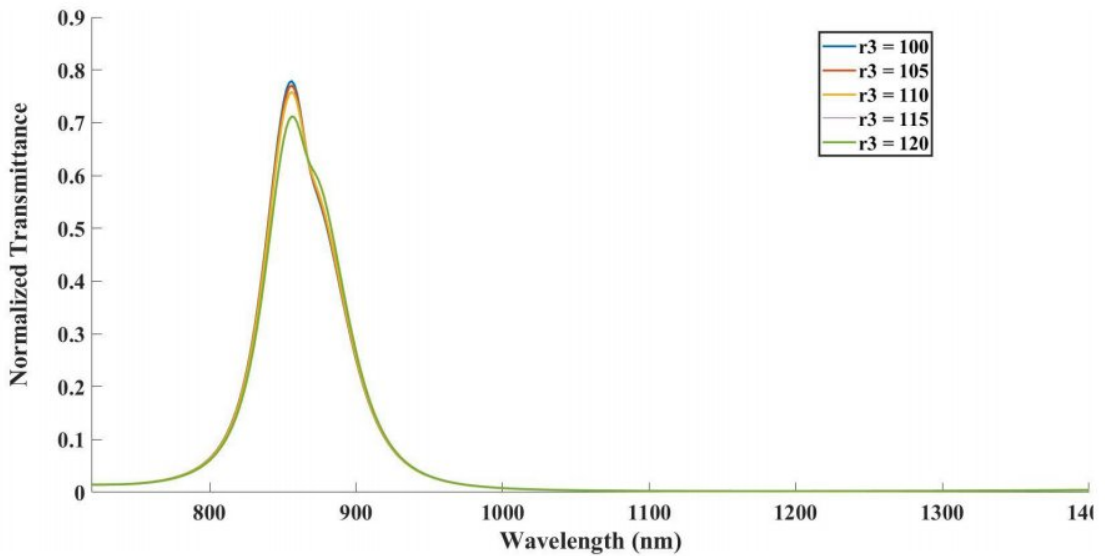


**Figure 5.32:** Variation of r3 for port 1

By repeating this process several times, the optimized parameters are found and the best possible transmission spectrum with high Q-factor is obtained. Figure 5. shows the improved transmission spectrum and the Table shows the quality factor for each ports.

The spacing between the two channels which is the channeling distance is also improved to 124 nm which is significantly higher than the initial obtained value. The

transmission peaks occur at 863 nm and 987 nm for port 1 and port 2 respectively. Greater channeling distance provides the advantage of selecting multiple channels within the demux.

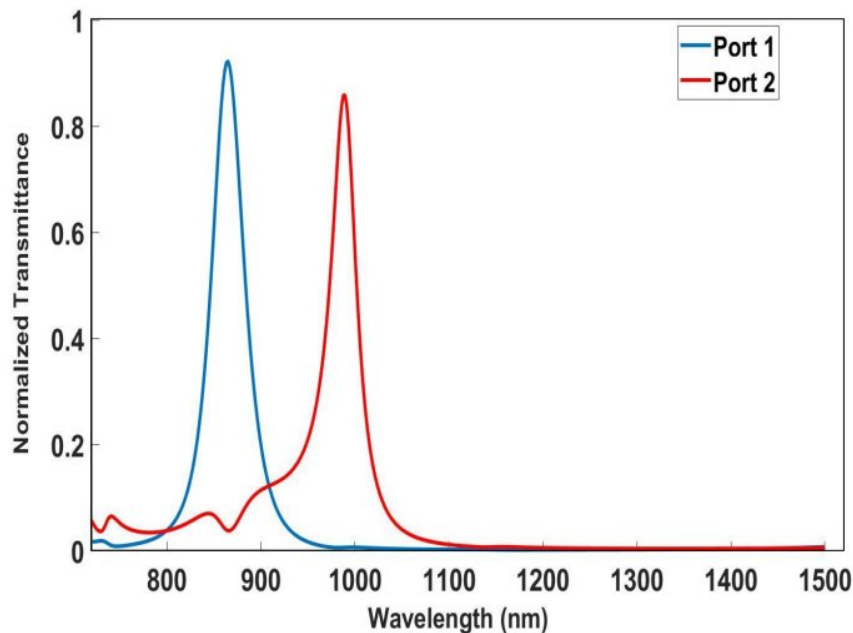


**Figure 5.33:** Improved channeling and Q-factor

Port name	Q - factor
Port 1 (Blue)	22
Port 2 (Red)	25

**Table 5.6:** Improved Q-factor

# Chapter 6

## Conclusion and Future Work

### 6.1 Conclusion

The research focused on producing highly effective devices with good lifetime. It was achieved for the plasmonic structures. The sensor had a low transmission peak, but it can be amplified due to present technology. Filter and demultiplexers had much better results with the filter reaching a very low dip in the 0.01 range. As a result, it can be said that, the objectives previously stated have been completed.

### 6.2 Future Work

Most of the works proposed here have only been simulated. As a result, the physical implications of fabricating it in the real world is unknown. So, fabrication should be tested before further progress.

Also the structures can be tested for multiple fields and see whether they give optimal results or not. Fields like: biosensing, pressure sensing, chemical sensing can be explored to test the full performance of the sensors

As for demultiplexers and filters, the fabricated structures should be used in real life applications whether in data calculation and calibration.

In the end, the structures will have to go through multiple hardware performance test so as to check the power losses matches with the simulated results or not.

## REFERENCES

- [1] S. Khani, M. Danaie, and P. Rezaei, "Realization of single-mode plasmonic band-pass filters using improved nanodisk resonators," *Optics Communications*, vol. 420, pp. 147–156, 2018.
- [2] H. Liu, Y. Gao, B. Zhu, G. Ren, and S. Jian, "A t-shaped high resolution plasmonic demultiplexer based on perturbations of two nanoresonators," *Optics Communications*, vol. 334, pp. 164–169, 2015.
- [3] A. H. . H. B. S. Hocine Bahri, Souheil Mouetsi, "A high sensitive sensor using mim waveguide coupled with a rectangular cavity with fano resonance," *Opt Quant Electron*, vol. 53, p. 332, 2021.
- [4] M. F. Hassan, R. H. Sagor, I. Tathfif, K. S. Rashid, and M. Radoan, "An optimized dielectric-metal-dielectric refractive index nanosensor," *IEEE Sensors Journal*, vol. 21 number=2, pages=1461–1469, year=2020.
- [5] D. Niu, X. Wang, S. Sun, M. Jiang, Q. Xu, F. Wang, Y. Wu, and D. Zhang, "Polymer/silica hybrid waveguide temperature sensor based on asymmetric mach–zehnder interferometer," *Journal of Optics*, vol. 20, no. 4, p. 45803, 2018.
- [6] A. A. Y. I. T. Kazi Sharmeen Rashid, Md. Farhad Hassan and R. H. Sagor, "Gas-sensing and label-free detection of biomaterials employing multiple rings structured plasmonic nanosensor," *Sensing and Bio-Sensing Research*, vol. 33, p. 100440, 2021.
- [7] Y. Kong, P. Qiu, Q. Wei, W. Quan, S. Wang, and W. Qian, "Refractive index and temperature nanosensor with plasmonic waveguide system," *Optics Communications*, vol. 371, pp. 132–137, 2016.
- [8] M. O. F. . R. H. S. Rabiul Al Mahmud, "Plasmonic refractive index sensor based on ring-type pentagonal resonator with high sensitivity," vol. 16, pp. 873–880, 2021.

- [9] X. L. D. M. Guoxi Wang, Hua Lu and L. Duan, "Tunable multi-channel wavelength demultiplexer based on mim plasmonic nanodisk resonators at telecommunication regime," *Opt. Express*, vol. 19, pp. 3513–3518, 2011.
- [10] A. F. . A. M. Shiva Khani, "Reconfigurable and scalable 2,4-and 6-channel plasmonics demultiplexer utilizing symmetrical rectangular resonators containing silver nano-rod defects with fdtd method," *Sci Rep*, vol. 11, p. 13628, 2021.
- [11] L.-L. W. Y.-F. Z. G.-Y. D. Zhao Chen, Li Yu and J.-H. Xiao, "High-resolution compact plasmonic wavelength demultiplexers based on cascading square resonators," *Chinese Physics Letters*, vol. 30, p. 054212, 2013.
- [12] Z. Chen, L. Yu, L. Wang, G. Duan, Y. Zhao, and J. Xiao, "A refractive index nanosensor based on fano resonance in the plasmonic waveguide system," *IEEE Photonics Technology Letters*, vol. 27, no. 16, pp. 1695–1698, 2015.
- [13] J. M. E. A D Rakic, A B Djuricic and M. L. Majewski, "Optical properties of metallic films for vertical-cavity optoelectronic devices," *Applied optics*, vol. 37, no. 22, pp. 5271–5283, 1998.
- [14] J. Zhang, L. Zhang, and W. Xu, "Surface plasmon polaritons: physics and applications," *Journal of Physics D: Applied Physics*, vol. 45, no. 11, p. 113001, 2010.
- [15] T. W. E. William Barnes, Alain Dereux, "Surface plasmon subwavelength optics," *Nature*, vol. 424, no. 6950, pp. 824–830, 2003.
- [16] A. V. Zayats, I. I. Smolyaninov, and A. A. Maradudin, "Nano-optics of surface plasmon polaritons," *Physics Reports*, vol. 408, no. 3–4, pp. 131–314, 2005.
- [17] H. C. Zhang, P. H. He, W. X. Tang, Y. Luo, and T. J. Cui, "Planar spoof spp transmission lines, applications in microwave circuits," *IEEE Microwave Magazine*, vol. 20, no. 11, pp. 73–91, 2019.
- [18] T. Wu, Y. Liu, Z. Yu, H. Ye, Y. Peng, C. Shu, C. Yang, W. Zhang, and H. He, "A nanometric temperature sensor based on plasmonic waveguide with an ethanol-sealed rectangular cavity," *Optics Communications*, vol. 339, pp. 1–6, 2015.
- [19] A. A. Y. E. S. . M. I. A. Rakibul Hasan Sagor, Md. Farhad Hassan, "Highly sensitive refractive index sensor optimized for blood group sensing utilizing the fano resonance," *Applied Nanoscience*, vol. 21, pp. 521–534, 2021.
- [20] S. O. . M. S. Pardis Palizvan, "An optical mim pressure sensor based on a double square ring resonator," *Photonic Sensors*, vol. 8, pp. 242–247, 2020.
- [21] C. R. L. N. . M. G. Berini, P., "Characterization of long-range surface-plasmon-polariton waveguides," *Journal of Applied Physics*, vol. 98, no. 4, p. 43109, 2005.



- [22] R. Salvador, A. Martinez, C. Garcia-Meca, R. Ortuno, and J. Marti, "Analysis of hybrid dielectric plasmonic waveguides," *IEEE Journal of Selected Topics in Quantum Electronic*, vol. 14, no. 6, pp. 1496–1501, 2008.
- [23] P. Magarshack and P. G. Paulin, "System-on-chip beyond the nanometer wall," *Laser Physics*, vol. 30, no. 2, p. 026204, 2019.
- [24] J. N. D. . R. Jha, "Highly sensitive d shaped pcf sensor based on spr for near ir," *Opt Quant Electron*, vol. 48, p. 137, 2016.
- [25] S. M. R. Harikesavan Thenmozhi and K. Ahmed, "D-shaped pcf sensor based on spr for the detection of carcinogenic agents in food and cosmetics," *Optik*, vol. 180, pp. 264–270, 2019.
- [26] M. A. . M. D. Mahdiye Rahmatiyar, "Design of a refractive index plasmonic sensor based on a ring resonator coupled to a mim waveguide containing tapered defects," *Plasmonics*, vol. 15, pp. 2169–2176, 2020.
- [27] M. A. Butt, S. N. Khonina, and N. L. Kazanskiy, "Plasmonic refractive index sensor based on metal–insulator-metal waveguides with high sensitivity," *Journal of Modern Optics*, vol. 66, no. 9, pp. 1038–1043, 2019.
- [28] ———, "Plasmonic refractive index sensor based on m-i-m square ring resonator," in *2018 International Conference on Computing, Electronic and Electrical Engineering (ICE Cube)*, 2018, pp. 1–4.
- [29] Y. Z. . M. Cui, "Refractive index sensor based on the symmetric mim waveguide structure," *J. Electron. Mater.*, vol. 48, pp. 1005–1010, 2019.
- [30] X. Zhao, Z. Zhang, and S. Yan, "Tunable fano resonance in asymmetric mim waveguide structure," *Sensors*, vol. 17, no. 7, p. 1497, 2017.
- [31] X. Z. Y. C. L. W. Y. Z. . L. Y. Yunyun Zhang, Shilei Li, "Evolution of fano resonance based on symmetric/asymmetric plasmonic waveguide system and its application in nanosensor," *Optics Communications*, vol. 370, pp. 203–208, 2016.
- [32] F. B. Z. . A. S. A. Maryam Bazgir, Majid Jalalpour, "Design of an optical switch and sensor based on a mim coupled waveguide using a dna composit," *J. Electron. Mater.*, vol. 49, pp. 2173–2178, 2020.
- [33] L. C. J. Z. L. L. . Z. M. Kunhua Wen, Yihua Hu, "Single/dual fano resonance based on plasmonic metal-dielectric-metal waveguide," *Plasmonics*, vol. 11, pp. 315–321, 2016.
- [34] J. Yang, X. Song, S. Yang, L. Cui, and L. Yu, "Independently controllable multiple fano resonances in side-coupled mdm structure and its applications for sensing and wavelength demultiplexing," *Journal of Physics D: Applied Physics*, vol. 5, no. 3, p. 321507, 2017.

- [35] N. Amosoltani, N. Yasrebi, A. Farmani, and A. Zarifkar, "A plasmonic nano-biosensor based on two consecutive disk resonators and unidirectional reflection-less propagation effect," *IEEE Sensors Journal*, vol. 20, no. 16, pp. 9097–9104, 2020.
- [36] X. W. X. W. Y. W. Y. S. H. T. Y. Q. Xiangxian Wang, Jiankai Zhu and H. Yang, "Wide range refractive index sensor based on a coupled structure of au nanocubes and au film," *Optical Materials Express*, vol. 9, no. 7, pp. 3079–3088, 2019.
- [37] J. Yu, J. Zhu, S. Ye, and X. Wang, "Ultra wide sensing range plasmonic refractive index sensor based on nano-array with rhombus particles," *Chinese Physics B*, vol. 29, no. 11, p. 114204, 2020.
- [38] T. Xu, Z. Geng, and Y. Su, "A potential plasmonic biosensor based asymmetric metal ring cavity with extremely narrow linewidth and high sensitivity," *Sensors*, vol. 21, no. 3, p. 752, 2021.
- [39] L. Singh, N. Agrawal, and C. Saha, "Investigation of glucose sensor by using plasmonic mim waveguide based m," in *2021 IEEE MTT-S International Microwave and RF Conference (IMARC)*, 2021, pp. 1–4.
- [40] L. C. J. Z. M. H. L. L. . Z. M. Kunhua Wen, Yihua Hu, "Tunable multimode plasmonic filter based on asymmetric dual side-coupled u-shape cavities resonators," *Optik*, vol. 182, pp. 324–330, 2019.
- [41] H. Feng, Z. Liu, J. Zhang, L. Ran, and Y. Gao, "An ultra-high efficient plasmon waveguide filter with enhanced filtering effect," *Optics Communications*, vol. 499, p. 127287, 2021.
- [42] M. H. Mehedi Hasan, Ferdousi Mayoia and S. Islam, "Plasmonic corrugated waveguide coupled to a rectangular nano-resonator as an optical filter,," *OSA Continuum*, vol. 3, no. 12, pp. 3314–3323, 2020.
- [43] W. Zhao and Z. Lu, "Nanoplasmonic optical switch based on ga-si<sub>3</sub>n<sub>4</sub>-ga waveguide," *Opt. Eng.*, vol. 50, p. 074002, 2011.
- [44] S. Khani, M. Danaie, and P. Rezaei, "Realization of single-mode plasmonic band-pass filters using improved nanodisk resonators," *Opt. Commun.*, vol. 420, pp. 147–156, 2018.
- [45] G. H. . Y. C. Binfeng Yun, "Resonant mode analysis of the nanoscale surface plasmon polariton waveguide filter with rectangle cavity," *Plasmonics*, vol. 8, pp. 267–275, 2012.
- [46] M. R. R. . M. A. Mansouri-Birjandi, "Utilizing the metallic nano-rods in hexagonal configuration to enhance sensitivity of the plasmonic racetrack resonator in sensing application," *Plasmonics*, vol. 12, pp. 999–1006, 2016.

- [47] S. Khani, M. Danaie, and P. Rezaei, "Size reduction of mim surface plasmon based optical bandpass filters by the introduction of arrays of silver nano-rods," *Physica E: Low-dimensional Systems and Nanostructures*, vol. 113, pp. 25–34, 2019.
- [48] G. H. . Y. C. Binfeng Yun, "Resonant mode analysis of the nanoscale surface plasmon polariton waveguide filter with rectangle cavity," *IEEE Transactions on Nanotechnology*, vol. 8, no. 2, pp. 267–275, 2013.
- [49] X. H. Jin Tao and S. Liu, "Optical characteristics of surface plasmon nanonotch structure," *J. Opt. Soc. Am.*, vol. 27, pp. 1430–1434, 2010.
- [50] Y. Wang, Y.-Y. Xie, Y.-C. Ye, Y.-X. Du, B.-C. Liu, W.-J. Zheng, and Y. Liu, "Exploring a novel approach to manipulating plasmon-induced transparency," *Optics Communications*, vol. 427, pp. 505–510, 2018.
- [51] X.-S. L. J. T. Qin Zhang, Xu-Guang Huang and X.-P. Jin, "A subwavelength coupler-type mim optical filter," *Optical Express*, vol. 17, pp. 7549–7554, 2009.
- [52] H. J. H. S.-H. C. T. S. K. . H.-P. C. Yuan-Fong Chou Chau, Chung-Ting Chou Chao, "A multichannel color filter with the functions of optical sensor and switch," *Sci Rep*, vol. 11, p. 22910, 2021.
- [53] J. Zhang, H. Feng, and Y. Gao, "Plasmonic narrowband filter based on an equilateral triangular resonator with a silver bar," *Photonics*, vol. 8, p. 244, 2021.
- [54] F. Abdolalipour and M. Pourmahyabadi, "High q-factor plasmonic filter based on mim structures and its application in the design of a dual band demultiplexer for optical communication wavelengths," *J. Opt. Soc. Am. B*, vol. 39, pp. 364–372, 2022.
- [55] A. Yariv, "Universal relations for coupling of optical power between microresonators and dielectric waveguides," *Electronics Letters*, vol. 36, no. 4, pp. 321–322, 2000.
- [56] J. Zhu and J. Lou, "High-sensitivity fano resonance temperature sensor in mim waveguides coupled with a polydimethylsiloxane-sealed semi-square ring resonator," *Results in Physics*, vol. 18, p. 103183, 2020.